HHS Public Access

Author manuscript

Cell. Author manuscript; available in PMC 2024 April 12.

Published in final edited form as:

Cell. 2024 March 28; 187(7): 1666–1684.e26. doi:10.1016/j.cell.2024.02.023.

First-in-class MKK4 inhibitors enhance liver regeneration and prevent liver failure

Stefan Zwirner[1,2,18], **Anan A. Abu Rmilah**[3,18], **Sabrina Klotz**[1,18], **Bent Pfaffenroth**[4], **Philip Kloevekorn**[4], **Athina A. Moschopoulou**[1], **Svenja Schuette**[1], **Mathias Haag**[5], **Roland Selig**[2,4], **Kewei Li**[3], **Wei Zhou**[3], **Erek Nelson**[3], **Antti Poso**[1,6,7], **Harvey Chen**[3], **Bruce Amiot**[3], **Yao Jia**[3], **Anna Minshew**[3], **Gregory Michalak**[3], **Wei Cui**[1], **Elke Rist**[1], **Thomas Longerich**[8], **Birgit Jung**[2], **Philipp Felgendreff**[3], **Omelyan Trompak**[1], **Prem K. Premsrirut**[9], **Katharina Gries**[1], **Thomas E. Muerdter**[5], **Georg Heinkele**[5], **Torsten Wuestefeld**[10,11,19], **David Shapiro**[2], **Markus Weissbach**[2], **Alfred Koenigsrainer**[7,12,13], **Bence Sipos**[1], **Eiso AB**[14], **Magdalena Ortiz Zacarias**[14], **Stephan Theisgen**[14], **Nicole Gruenheit**[15], **Saskia Biskup**[15], **Matthias Schwab**[5,7,16], **Wolfgang Albrecht**[2], **Stefan Laufer**[4,17,18,*], **Scott Nyberg**[3,18,*], **Lars Zender**[1,7,12,17,18,20,*]

[1]Department of Medical Oncology and Pneumology (Internal Medicine VIII), University Hospital Tübingen, Tübingen 72076, Germany

[2]HepaRegeniX GmbH, Tübingen 72072, Germany

[3]William J. von Liebig Center for Transplantation and Clinical Regeneration, Mayo Clinic, Rochester, MN 55905, USA

[4]Department of Pharmaceutical Chemistry, University of Tübingen, Tübingen 72076, Germany

[5]Dr. Margarete Fischer-Bosch Institute of Clinical Pharmacology, Stuttgart 70376, Germany

[6]School of Pharmacy, University of Eastern Finland, Kuopio 70211, Finland

[7]iFIT Cluster of Excellence (EXC 2180) “Image-guided and Functionally Instructed Tumor Therapies”, University of Tübingen, Tübingen 72076, Germany

[*]Correspondence: stefan.laufer@uni-tuebingen.de (S.L.), nyberg.scott@mayo.edu (S.N.), lars.zender@med.uni-tuebingen.de (L.Z.).

AUTHOR CONTRIBUTIONS

L.Z., W.A., S.L., and S.N. conceptualized and designed the study. L.Z., S.Z., A.A.A.R., S.K., B.J., B.P., P.K., A.M., S.S., M.H., R.S., K.L., W.Z., E.N., A.P., H.C., B.A., Y.J., A.M., G.M., W.C., E.R., T.L., P.F., O.T., P.K.P., T.W., B.S., M.S., W.A., S.L., E.A, M.O.Z., S.T., and S.N. provided technical, methodological, material support, and resources. L.Z., S.Z., A.A.A.R., S.K., B.P., P.K., A.M., S.S., M.H., R.S., K.L., W.Z., E.N., A.P., H.C., B.A., Y.J., A.M., G.M., W.C., T.L., P.F., O.T., P.K.P., T.W., B.S., M.S., W.A., S.L., E.A, and S.T. contributed to the acquisition of data, and L.Z., B.P., S.Z., A.A.A.R., S.K., E.A., M.S., W.A., and S.L. analyzed and interpreted the results. L.Z., S.Z., A.A.A.R., S.K., B.P., P.K., A.M., S.S., M.H., R.S., K.L., W.Z., E.N., A.P., H.C., B.A., Y.J., A.M., G.M., W.C., T.L., P.F., O.T., P.K.P., T.W., B.S., M.S., W.A., and S.L. provided formal analysis of the data and data curation. L.Z., S.L., and M.S. acquired funding for the study. L.Z. prepared the first manuscript, and S.N., W.A., S.L., S.Z., and L.Z. revised and edited the manuscript. W.A., M.W., and L.Z. performed all phase-I-study-related statistical analyses and had unrestricted access to all phase I study data. All authors agreed to submit the manuscript, read, and approved the final draft and take full responsibility of its content, including the accuracy of the data and the fidelity of the trial to the registered protocol and its statistical analysis.

DECLARATION OF INTERESTS

L.Z. and T.W. are co-inventors of the patent WO 2012/136859. L.Z., S.L., and A.P. are founders, shareholders, and scientific advisors of HepaRegeniX (HRX) GmbH. B.J., D.S., and M.W. are advisors of HRX. W.A., R.S., and S.Z. are employees of HRX. E.A.B., M.O.Z., and S.T. are employees of ZoBio. M.S. received research support and funding from Green Cross WellBeing Co. Ltd., Gilead Sciences Inc., Robert Bosch GmbH, CORAT Therapeutics GmbH, Agena Bioscience, HepaRegeniX GmbH, and CED Services GmbH.

[8]Institute of Pathology, University Hospital Heidelberg, Heidelberg 69120, Germany

[9]Mirimus Inc, 760 Parkside Ave, Brooklyn, NY 11226, USA

[10]Laboratory for In Vivo Genetics & Gene Therapy, Genome Institute of Singapore, Agency for Science, Technology and Research (A*STAR), Singapore 138672, Singapore

[11]School of Biological Sciences, Nanyang Technological University of Singapore, Singapore 637551, Singapore

[12]German Cancer Research Consortium (DKTK), German Cancer Research Center (DKFZ), Heidelberg 69120, Germany

[13]Department of General-, Visceral, and Transplant Surgery, University Hospital Tübingen, Tübingen 72076, Germany

[14]ZoBio B.V., Leiden 2333 CH, the Netherlands

[15]CeGaT GmbH, Tübingen 72076, Germany

[16]Department of Clinical Pharmacology, Pharmacy and Biochemistry, University of Tübingen, Tübingen 72076, Germany

[17]Tübingen Center for Academic Drug Discovery & Development (TüCAD2), Tübingen 72076, Germany

[18]These authors contributed equally

[19]Present address: Lee Kong Chian School of Medicine, Nanyang Technological University of Singapore, Singapore 637551, Republic of Singapore

[20]Lead contact

SUMMARY

Diminished hepatocyte regeneration is a key feature of acute and chronic liver diseases and after extended liver resections, resulting in the inability to maintain or restore a sufficient functional liver mass. Therapies to restore hepatocyte regeneration are lacking, making liver transplantation the only curative option for end-stage liver disease. Here, we report on the structure-based development and characterization (nuclear magnetic resonance [NMR] spectroscopy) of first-in-class small molecule inhibitors of the dual-specificity kinase MKK4 (MKK4i). MKK4i increased liver regeneration upon hepatectomy in murine and porcine models, allowed for survival of pigs in a lethal 85% hepatectomy model, and showed antisteatotic and antifibrotic effects in liver disease mouse models. A first-in-human phase I trial (European Union Drug Regulating Authorities Clinical Trials [EudraCT] 2021-000193-28) with the clinical candidate HRX215 was conducted and revealed excellent safety and pharmacokinetics. Clinical trials to probe HRX215 for prevention/treatment of liver failure after extensive oncological liver resections or after transplantation of small grafts are warranted.

Graphical Abstract

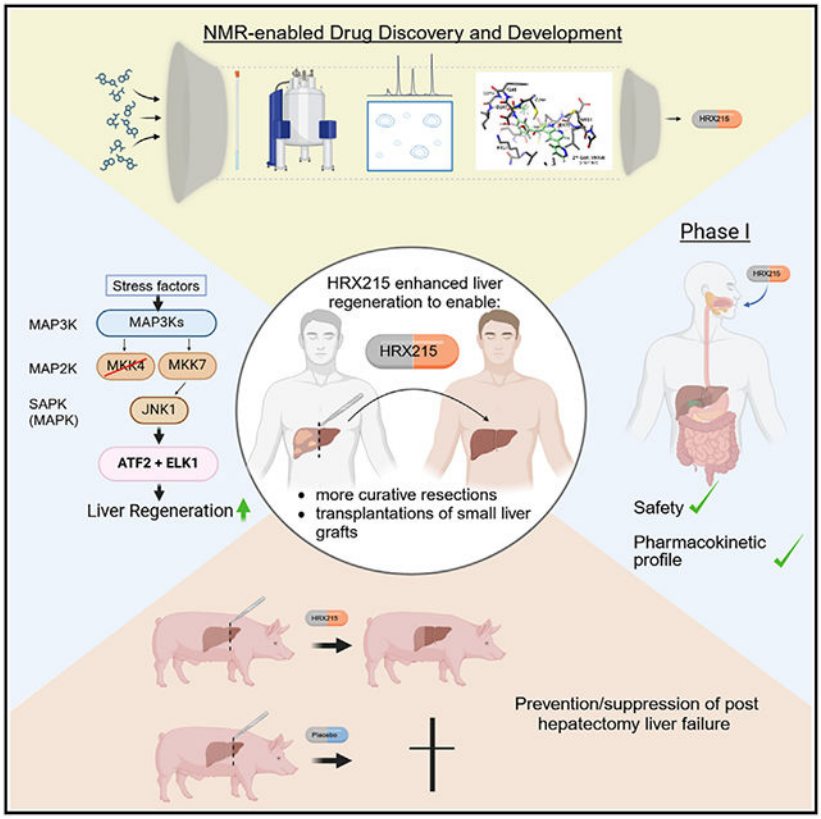

In brief

A targeted therapy against the kinase MKK4 was developed (HRX215) and investigated preclinically, as well as in a phase I study in humans. HRX215 boosted liver regeneration, prevented liver failure after extensive hepatectomy in pigs, and holds the promise to prevent liver failure after extensive oncological liver resections or transplantation of small liver grafts in humans.

INTRODUCTION

Liver diseases represent a major and increasing health problem accounting for more than two million deaths per year worldwide.[1] The number of deaths due to liver diseases has increased by 50% in the past three decades and is predicted to double in the next 20 years.[2]

One key feature of acute and chronic liver diseases and after extended liver resections is the inability of hepatocytes to sufficiently regenerate and restore or maintain a critical functional liver mass. Although healthy livers harbor a nearly unlimited regenerative potential, damage-associated changes in the hepatic microenvironment of acutely or chronically injured livers diminish the hepatocytes' regenerative capacity.[3] Unfortunately, the underlying molecular mechanisms are poorly understood.

We recently reported on the discovery of the dual specific kinase MKK4 as a master regulator of hepatocyte regeneration.[4] MKK4 is a MAP2 kinase and part of the stress-

activated protein kinase (SAPK)/mitogen-activated protein kinase (MAPK) signaling networks.[5,6] MKK4 can be activated upon a cell's exposure to different stress stimuli. Downstream substrates of MKK4 are JNK 1, 2, and 3, which are also activated by MKK7, and the p38 MAPK isoforms, which, however, are primarily activated by MKK3 and MKK6.[7] Short hairpin RNA (shRNA)mir-mediated silencing of MKK4 was found to unlock endogenous regenerative capacity of hepatocytes in acutely or chronically injured livers via derouting SAPK signaling predominantly through MKK7 and JNK1 toward a downstream pro-regenerative transcriptional program mediated by ATF2 and ELK1.[4] Unfortunately, no small molecule inhibitors for selective MKK4 inhibition are available.

We here report on the development and *in vitro* and *in vivo* characterization of first-in-class small molecule inhibitors of the dual specific kinase MKK4 (MKK4i). MKK4i increased liver regeneration upon hepatectomy in murine and porcine models. Strikingly, treatment with the clinical candidate HRX215 prevented posthepatectomy-liver-failure (PHLF) and allowed for the survival of pigs in a lethal 85% hepatectomy model, suggesting that boosted liver regeneration by HRX215 might represent a viable treatment option for human PHLF and the pathogenetically related small for-size syndrome (SFSS) after liver transplantation.

Testing of HRX215 in a phase I trial in 48 healthy volunteers revealed excellent safety, tolerability, and pharmacokinetics (PKs) of HRX215. Clinical trials to probe HRX215 as a therapeutic option to prevent/treat liver failure after extensive oncological liver resections or after transplantation of small liver grafts are warranted.

RESULTS

Drug discovery and development is a demanding process, and reliable methods to predict the feasibility and safety of systemic pharmacotherapies are lacking. To mimic the systemic action of MKK4 inhibitors along with assessing tolerability and safety, we engineered MKK4 shRNA transgenic mice via recombinase-mediated cassette exchange (RMCE) insertion of a tet-responsive element (TRE)-driven shRNAmir cassette into the *Col1a1* locus, as previously described.[8] Expression of a GFP-linked shRNA targeting *MKK4* ora non-targeting control shRNA (shNC) is controlled by a TRE promoter. TRE-shMKK4 mice were crossed to mice constitutively expressing the reverse tet-transactivator[9,10] (Figure 1A). When compound mutant mice were dosed with doxycy-cline (dox), marked GFP expression could be observed in intestine, liver, kidney, muscle, and pancreas (Figure 1B). Intermediate GFP expression was found in heart, lung, and spleen, whereas no GFP expression was found in the brain (Figure 1B). Functionality of the GFP-linked MKK4 shRNA was shown by western blotting of lysates from liver (Figure 1C) and other tissues (Figure S1A). When dox-treated CAG-rtTA; TRE-shMKK4 mice were subjected to partial hepatectomy, the number of proliferating hepatocytes was significantly higher compared with CAG-rtTA3; TRE-shNC mice (Figures 1D–1F), corroborating our previous results[4] that genetic MKK4 suppression in hepatocytes enhances liver regeneration.

To assess the safety of prolonged systemic MKK4 suppression, mice were kept on dox for 12 months. All investigated animals showed normal body weight development (Figure 1G). Histopathological evaluation of liver, heart, lung, pancreas, kidney, spleen,

and intestine did not reveal any morphological evidence of toxicity (Figure 1H), a finding that is well in line with the fact that MKK4 is only activated through phosphorylation under stress conditions[11,12] (Figure S1B). In summary, our data demonstrate that sustained systemic MKK4 suppression is well tolerated and does not result in increased spontaneous tumorigenesis within the observation period, confirming previous results from a comprehensive set of classical *in vitro* and *in vivo* transformation assays.[4] Nevertheless, we aimed to probe potential pro-tumorigenic risks associated with MKK4 suppression under the most stringent conditions. Fumarylacetoacetate-hydrolase (FAH) knockout mice show increased rates of spontaneous liver tumorigenesis, even after genetic reconstitution with a wild-type *Fah* transgene in hepatocytes.[13,14] Taking advantage of a recently established *in vivo* platform,[4] we repopulated livers of $Fah^{-/-}$ mice from hepatocytes stably expressing MKK4-shRNAs or non-coding control shRNAs (Figure S1C). Mice were exposed to a choline-deficient high-fat diet (CD-HFD) (Figure S1C), which was reported to induce nonalcoholic steatohepatitis (NASH) and NASH hepatocellular carcinoma (HCC).[15] Importantly, we found similar frequencies of dysplastic nodules (Figure S1D) and HCCs (Figures S1E and S1F) in livers with MKK4 suppression and control livers, suggesting that MKK4 silencing does neither fuel tumor initiation nor tumor progression in this system. In accordance, we did not detect survival differences of mice with stable intrahepatic MKK4 knockdown vs. control mice (Figure S1G). When non-alcoholic fatty liver disease (NAFLD) activity scoring (NAS) was applied to non-tumorigenic parts of both livers, no differences were found in this combined FAH repopulation/CD-HFD system (Figure S1H), which shows a higher penetrance of HCC development than CD-HFD in wild-type mice.[15] Collectively, these data support the concept of boosting liver regeneration by MKK4 inhibition without the risk of increased liver tumorigenesis.

Encouraged by these results, we initiated a drug discovery process. MKK4 represents an unexplored therapeutic target and despite its central function in the SAPK/MAPK pathways, valuable information regarding the conformational structure of the protein or activity-modulating ligands was not available. Crystal structures of the kinase domain have been disclosed;[16,17] however, the resolution was insufficient for the development of a robust binding model.

We conducted co-crystallization experiments (kinase domain, amino acids [aa] 80–399) with metal additives, which led to the isolation of crystals, which showed acceptable diffraction patterns and a resolution in the range of 2.5 and 3.0Å, similar to those previously published.[16,17] However, although the co-crystallized ATP analog adenylyl imidodiphosphate (AMP-PNP) was clearly identified, a detected moderate anisotropy prevented an accurate determination of the ligand binding poses (Figures S2A and S2B).

As an exploitable ATP-binding pocket model could not be established, a literature search focusing on reported off-target profiles of protein kinase inhibitors was conducted and revealed an MKK4 inhibitory potential of the clinically approved $BRAF^{V600E}$ inhibitor vemurafenib.[18] The reported high binding affinity of vemurafenib was confirmed by employing the Eurofins/DiscoverX KINOMEscan platform (K_D = 13.5 nM) (Figure S2C). Using a kinase assay, vemurafenib was found to inhibit the pMKK4-mediated phosphorylation of JNK1 with an IC_{50} value of 0.8 μM (Figure S2D). To investigate

whether MKK4 activation is modulated upon binding of the compound, a cascade assay was developed (Figure 2A) (see STAR Methods for a detailed description), which revealed that vemurafenib has a dual mode of action on MKK4. It inhibits MKK4 activation (IC_{50} value of 7 μM) (Figure 2B, orange line) and at the same time suppresses phosphorylation of MKK4 downstream targets.

Vemurafenib inhibits mutated $BRAF^{V600E}$, and except for interactions with A-, B-, and C-Raf, MAP4K5, SRMS, and ACK1, it harbors a good kinome selectivity. Besides an improvement of potency against MKK4, further objectives were to remove the affinity to the Raf-kinase motif and to substantially improve the selectivity over JNK1 and MKK7 because both are critical off-targets that play a crucial role in mediating the pro-regenerative effect upon MKK4 silencing.[4]

The chemical structure of vemurafenib was dissected as shown in Figure 2C. The carbonyl linker and the alkyl sulfonyl group are crucial for MKK4 inhibition. After verification that the pyrazolo pyridine ring represents an attractive second hinge-binding motif with very similar MKK4-binding and slightly better inhibition properties (Figures S2E and S2F), both bicyclic structures were used in parallel for lead optimization. Details of chemical approaches for modifying the alkyl sulfonamide and C-ring substitutions have been published.[19,20] Replacement of the sulfonamide by an amide group resulted in a complete loss of MKK4-affinity and the variation of the alkyl chain length (C_1-C_6), and the introduction of the haloalkyl, phenyl, benzyl, and methoxyethyl group demonstrated that n-propyl or benzyl-sulfonamide is preferred to maximize MKK4-binding affinity.[20] C-Ring modifications revealed a substantial advantage of N-heterocycles over the original para-chlorophenyl or other mono- or disubstituted phenyl groups, which finally led to the identification of LN3117 and LN3118 with IC_{50}-values of 138 and 200 nM for MKK4 (Figures S2G and S2H). Both compounds showed good oral bioavailability in the mouse, but the n-propyl sulfonamide group in LN3117 was less susceptible to metabolic clearance, which led to a substantially slower systemic elimination (Figures S2G and S2H). However, in KINOMEScan, a strong BRAF-binding affinity was observed for LN3117, whereas LN3118 showed excellent selectivity over BRAF, JNK1, and MKK7 (Figures S2G and S2H) and was therefore selected as tool compound. Deibler et al. suggested a binding model for the vemurafenib analog PLX-4720 with key interactions between the sulfonamide oxygen and the backbone amide of Arg110, as well as one of the fluorine atoms and Lys131[21]; however, no conclusions regarding the exact binding site geometry could be drawn. As such information is prerequisite for lead optimization, we decided for nuclear magnetic resonance (NMR)-based structure elucidation. Due to the low aqueous solubility, tool compound LN3118 and its analog LN3117 were not appropriate ligands for analysis, and instead, compound LN3162 was used. In LN3162, a 2,6-fluoro-substitution was introduced, which resulted in a strong selectivity vs. BRAF (IC_{50}: 10 μM [BRAF] vs. 0.187 μM [MKK4]) (Figure S2I) and was therefore maintained in our lead optimization program.

Using the ^{2}H,^{15}N,^{13}C-labeled, 2-fold mutated kinase domain of MKK4 (aa 80–399, [C297A, C282A]) with protonated methyl groups of Ile, Val, Leu, and Met (ILVM) residues in presence of LN3162 allowed us to collect protein ligand nuclear Overhauser effects (NOEs) to define the binding mode of LN3162. Resonance assignments for almost all ILVM

methyl groups in the vicinity of the ligand involved in protein ligand NOEs were obtained from a series of 13 single mutants of the relevant ILVM residues in combination with analysis of protein methyl-methyl NOE contacts. In total, 33 intermolecular NOEs were assigned between the ligand and methyl groups of residues I108, V116, V162, M178, L180, M181, and L236. Figure S2J shows intermolecular NOEs observed for ligand protons H02 and H15 and several methyl groups. Additionally, one strong NOE was tentatively assigned to ligand proton H02 and the backbone NH resonance of Met181 (see Figure S2I for ligand proton nomenclature).

A binding mode of LN3162 was elaborated (Figure 2D) based on intra-protein methyl-methyl and intermolecular protein ligand NOE cross-peaks, as well as available crystal structures of vemurafenib-bound BRAF and ZAK[22–24] (PDB: 3OG7, 4RZV, and 5HES). Several key vemurafenib interactions (shown in Figure 2D) were reproduced and found in agreement with the intermolecular NOEs. No NOE violations above 1Å were found for any of the BRAF- or ZAK-based models, and LN3162 matched the position of vemurafenib in the crystal structures within 0.5Å root-mean-square deviation (RMSD). The model based on template 5HES chain A, shown in Figure S2K, with the protein ligand NOEs as dashed lines, displayed only a single NOE violation of 0.42Å but no other violations larger than 0.3Å and was selected as the representative model. The stability of the binding mode was checked and confirmed by short (10 ns) molecular dynamics simulations in presence of explicit solvent. Dashed lines in Figure 2D illustrate the azaindole-hinge and the sulfonamide-DFG-loop interactions, Cys[246] exhibits H-bonds between the sulfhydryl-group and the fluorine in position 2, as well as between the sulfonamide-NH and the backbone. According to this model, binding of the carbonyl linker requires a network interaction involving two water molecules. Fixed orientations of the pyridazine ring, which is presumably exposed without any obvious interactions, and fluorine in position 6 of the phenyl ring were not postulated so that further lead optimization focused on empirically, structure-activity relationship-driven modifications at these positions. C-Ring modifications of both hinge-binding motifs resulted in a series of candidates with MKK4 inhibition potency in the two-digit nM-range. Based on the >100-fold selectivity against JNK1, BRAF, and MKK7 (Figure 2E), HRX215 was selected as a clinical candidate. The route of synthesis is illustrated in Figure S2L. To investigate the MKK4-inhibition potency in cells, peripheral blood mononuclear cells (PBMCs), isolated from buffy coats from healthy donors were pre-incubated with increasing concentrations of the MKK4 inhibitor, and lipopolysaccharide (LPS) was added to trigger SAPK signaling via TLR4[25] (Figure 2F). A potent and dose-dependent MKK4i-mediated reduction of pMKK4 levels was determined by western blotting (Figure 2F), confirming cell membrane permeability of our drug.

We next probed the pharmacokinetic properties of HRX215. After oral administration of 30 mg/kg, maximum concentration (C_{max}) values of 67.4 and 53.5 μM were achieved in wild-type mice, which were 1.8- and 1.4-fold higher than the C_{max} values determined for the equivalent dose of vemurafenib (Figure 2G). The elimination half-life of HRX215 in mice was 3.4–3.9 h, allowing further *in vivo* pharmacology profiling. We next investigated whether our candidate would increase hepatocyte proliferation after partial hepatectomy. Mice were dosed with HRX215 12 h prior and again immediately before surgery, and hepatocyte proliferation was determined via Ki67 staining (Figure 3A). Vehicle-treated

mice showed 4.93% proliferating hepatocytes, whereas mice treated with 0.4 and 2 mg/kg HRX215 showed proliferation rates of 15.38% and 15.15%, respectively (Figures 3B and 3C). When HRX215 was increased to 10 mg/kg, the number of proliferating hepatocytes could be further increased to 26.3% (Figure 3C), establishing a dose-response relationship. Of note, when HRX215 was administered to wildtype mice without manipulation, we did not observe an induction of hepatocyte proliferation or an increase of liver/body weight ratio, corroborating that activated stress signaling in hepatocytes is needed to unlock regeneration upon MKK4 silencing (Figures 3D–3G). MRNA sequencing and transcriptomic analyses were conducted on mRNA obtained from hepatectomized mouse livers with shRNA-mediated MKK4 knockdown vs. hepatectomized HRX215-treated mouse livers and revealed highly correlative gene expression profiles, underlining HRX215's selectivity (Figure 3H). Importantly, HRX215 was found to enhance hepatocyte proliferation upon partial hepatectomy in fibrotic mouse livers (Figures 3I–3M), suggesting that the presence of fibrosis per se does not interfere with the HRX215-mediated pro-regenerative mechanism.

Besides boosting hepatocyte proliferation, MKK4 inhibition stabilizes hepatocytes under conditions of liver damage.[4] To investigate HRX215's ability to protect hepatocytes from cell death, we used a model of CCl_4-induced liver damage (Figure 3N). Mice were dosed with HRX215 12 h prior and directly before CCl_4 administration, and hepatocyte death was quantified via TdT-mediated dUTP-biotin nick end labeling (TUNEL) staining. HRX215 significantly reduced hepatocyte death compared with vehicle-treated animals (Figures 3O and 3P). Interestingly, when different doses of HRX215 were tested, we did not find further reduction of hepatocyte death in the 10 and 2 mg/kg dose groups compared with the 0.4 mg/kg dose group (Figure 3O), suggesting that the maximum therapeutic effect is already achieved at 0.4 mg/kg.

We recently reported that shRNA-mediated knockdown of MKK4 in damaged livers results in rerouted SAPK signaling via MKK7 and JNK1, which subsequently activates an ATF2 and ELK1 dependent pro-regenerative program in hepatocytes.[4] These key-signaling events were confirmed when MKK4i dosed mice were subjected to partial hepatectomy (Figure 4A) and are likely to also contribute to the hepatocyte stabilizing phenotype of MKK4 inhibition.[26–28] However, additional signaling and gene expression changes, such as reduced p38- and p53 activation,[29] activation of nuclear factor κB (NF-κB) signaling,[30,31] and upregulation of the anti-apoptotic protein Bcl-XL (Figures 4A–4C), are likely to contribute to the observed hepatocyte stabilizing phenotype.

Last but not least, we also observed antisteatotic and antifibrotic efficacy when MKK4i was tested in models of alcoholic steatohepatitis (ASH) (Figures S3A–S3C) and chronic CCl_4 treatment-induced liver fibrosis (Figures S3D–S3G), respectively.

To characterize the safety of HRX215, we did complete blood counts on mice treated for 4 weeks with either HRX215 or vehicle. No significant changes were detected in any of the investigated parameters (Figures S4A–S4I). Furthermore, when plasma and liver samples from HRX215- and vehicle-treated groups were subjected to untargeted metabolomics, no safety relevant changes were detected. Distinct findings in the HRX215 treated group were

derived from an HRX215 metabolite (Figure 4D). Likewise, in liver tissues, only HRX215-derived metabolites could be annotated as distinct between the two groups (Figure 4E).

Nonalcoholic steatohepatitis (recently renamed in metabolic-dysfunction associated steatohepatitis[32]) represents a risk factor for liver cancer development. We therefore set out to probe HRX215 in the Gubra Amylin NASH (GAN)-NASH model, which has become a standard within the pharmaceutical industry to test new NASH drugs and also effects on NASH-associated HCC.[33,34] After 37 weeks intake of a GAN high-fat diet, mice were randomized and either treated with HRX215 or vehicle over a 12-week time period (Figure S4J). Neither enhanced hepatocyte proliferation (Figure S4L) nor any metabolism changes that would raise safety concerns of our drug were observed in this setting (Figures S4M and S4N), corroborating our results from non-steatotic mice (Figures 4D and 4E). Detected differences in metabolites between the HRX215- and vehicle-treated group were related to carnitines and hypoxanthines, offering a mechanistic explanation for the observed antisteatotic effects[35,36] (Figures S3A–S3C). We also quantified numbers of potentially protumorigenic senescent cells in NASH livers[33] but found no differences between HRX215- and vehicle-treated mice (Figures S4O and S4P).

We continued with long-term tumorigenesis studies in the same model. Mice were treated with the GAN-NASH diet, and at week 60, liver biopsies of the mice were taken. Mice fulfilling the NASH criteria (steatosis score ≥2 and fibrosis stage 3) were randomized to either the HRX215 or vehicle group. After 64 weeks, 20 mice were euthanized to determine the baseline HCC burden (Figures 4F–4H). Subsequently, during another 12 weeks on diet, mice were treated either with HRX215 or vehicle (Figure 4F), followed by tumor burden analyses. Although all livers harbored liver carcinomas (Figures 4I and 4J), HRX215 treatment did not result in a higher number of tumor nodules per liver when compared with baseline, as well as with the tumor burden in the vehicle-treated group (Figure 4G). Strikingly, a tendency toward a reduction of tumor size in the HRX215-treated group was found (Figure 4H). Because microscopic analysis of liver regions without macroscopically visible tumor burden did not reveal significant differences regarding the numbers of dysplastic premalignant lesions (Figure 4K), our data suggest that HRX215 inhibits the progression of already established tumors.

Interestingly, when non-tumor bearing parts of mouse livers were analyzed, we observed more animals with an improved NAS score and less animals with a worsened NAS score in the HRX215-treated group (Figure S5A). A significant reduction of the overall hepatic lipid content and a tendency toward reduction of hepatocytes containing lipid droplets were found (Figures S5B–S5D), whereas no reduction of hepatic inflammation and hepatocyte ballooning was observed (Figures S5E–S5G). Liver fibrosis was found reduced in HRX215 treated livers, but results missed statistical significance in this model (Figures S5H–S5L). Interestingly, although hepatocyte apoptosis and hepatocyte senescence were not different between both groups (Figures S5M, S5O, and S5P), HRX215 treatment resulted in a slightly increased hepatocyte proliferation (Figure S5N), which is in contrast to the investigated short-term NASH model (Figure S4L) and suggests that only in the long-term and more severe NASH model stress signaling can be derouted toward pro-regenerative signaling. In summary, our data suggest that pharmacological inhibition of MKK4 does not increase or

accelerate tumor development in the employed NASH-HCC model and even exerts a growth inhibitory effect on established tumors. Furthermore, the significant antisteatotic effect and tendency toward an antifibrotic effect could be of interest for future combination therapies studies in NASH.

Obviously, we aimed to understand why MKK4 inhibition leads to increased proliferation of normal hepatocytes, while at the same time hampering the growth of liver carcinomas. This observation is in line with the fact that SAPK/MAPK signaling is cell type specific, and differences between normal and transformed cells exist.[37,38] Nevertheless, to deeper characterize this phenomenon, we took advantage of two well-established murine liver carcinoma cell lines (*Nras*^{G12V} *Cdkn2a*$^{ARF-/-}$ HCC cells[39,40]; *Nras*^{G12V} *Trp53*$^{-/-}$ HCC cells[40]). We found significantly reduced cell proliferation upon exposure of the cells to HRX215 (Figures S6A–S6C), whereas similar rates of cell death were detected (Figures S6D and S6E). As described earlier[4] (Figure 4A), the pro-regenerative signaling in hepatocytes upon MKK4 inhibition depends on increased MKK7 and JNK1 signaling with a downstream activation of the transcription factors ATF2 and ELK1. Interestingly, when MKK4 was inhibited by HRX215 in liver carcinoma cells, we found a distinct signal transduction pattern (Figures S6F and S6G). Phosphoprotein antibody arraying and western blotting revealed that MKK7 and JNK1 were significantly downregulated upon MKK4 inhibition (Figures S6F–S6H), and ATF2 and ELK1 levels remained stable. Interestingly and unlike MKK4-inhibited hepatocytes (p38 downregulation), we found a strong activation of p38 in MKK4-inhibited liver cancer cells (Figures S6F and S6G). In line with p38's well-established role as a suppressor of the cell-cycle regulatory phosphatase CDC25C, we found downregulation of the CDC25C target Cyclin B1 and also downregulation of Cyclin D1, Cyclin A2, and the microtubule regulating protein stathmin (Figure S6I). Furthermore, we detected downregulation of the receptor tyrosine kinases EGFR and Her2 and the downstream kinases ERK1/2 upon HRX215 treatment of cancer cells (Figure S6J).

We next aimed to probe HRX215's capacity to enhance liver regeneration in a porcine hepatectomy model, which faithfully reflects liver regeneration in humans.[41] The pig hepatectomy model can be conducted with 80% or 85% liver resection (Figure 5A). While the 80% hepatectomy model is non-lethal,[42] 85% liver resection results in an acute and lethal PHLF.[42]

We first investigated HRX215 in the 80% hepatectomy model. Eight pigs were randomized for HRX215 or vehicle treatment. Intravenous administration of HRX215 (5 mg/kg) or vehicle followed every 12 h, starting 24 h before surgery (Figure 5B). Directly after surgery, pigs underwent liver volumetry via computed tomography (CT) (Figure 5C). CT imaging confirmed equal extents of resection, and remaining liver volumes were comparable to 158.3 ± 33.3 mL in the placebo-treated group and 160.5 ± 11.9 in the HRX215-treated group (Figure 5D). Strikingly, CT imaging 43 h after hepatectomy revealed a newly regenerated liver volume of only 160.0 ± 23.5 in the placebo group, whereas livers in the HRX215-treated group had already regenerated 251.8 ± 13.6 mL (Figure 5D). In accordance with these values, we determined a regeneration index (RI) 2.57 ± 0.11 in the HRX215 treated group vs. only 2.12 ± 0.1 in the placebo group (Figure 5D). Pigs were euthanized for tissue collection at the 43 h time point. Although much of the regeneration had already occurred

before, we still observed significantly increased hepatocyte proliferation in the HRX215 group compared with the placebo group (Figures 5D and 5E). In summary, these data suggest that HRX215-mediated suppression of MKK4 increases hepatocyte regeneration in a pig hepatectomy model.

85% hepatectomy in pigs results in a lethal PHLF with a collapse of liver protein synthesis, impaired hepatic metabolism, increase in bilirubin levels, and a subsequent increase of intracranial pressure (ICP).[41] Because PHLF and the pathogenetically related small-for-size syndrome (after liver transplantation) represent major clinical problems, we aimed to test HRX215's therapeutic potential in the 85% hepatectomy setting. The study was conducted with continuous monitoring of vital signs, electrocardiogram (ECG) recording, measurement of ICP, measurement of central venous pressure, and continuous measurement of all relevant blood parameters (Figure 6A). Pigs were randomized into two HRX215 treatment groups with treatment starting either 12 h before surgery (n = 6) or 12 h after surgery (n = 6), and a placebo group (n = 6). Strikingly, HRX215-treated pigs did not show an increase in ICP values after surgery, which is typical for the development of acute liver failure in humans (Figure 6B). Metabolic capacities of remnant livers were determined via quantification of plasma ammonia and bilirubin levels. HRX215 prevented an increase of plasma ammonium (Figure 6C). Although bilirubin plasma levels continuously rose in the placebo group, there was only a transient rise with a subsequent drop in the HRX215-treated group (Figure 6D). The international normalized ratio (INR) reflects the liver's capacity to synthesize blood coagulation proteins, and we found that INR values in the HRX215-treated group only transiently rose above 1, whereas sustained values of up to 1.6 were found in the placebo group (Figure 6E). In line with these results, aspartate aminotransferase, a transaminase that indicates severe liver damage, was only transiently increased after surgery in the HRX215 treatment group, whereas levels remained above 800 U/L in the placebo group, indicating acute liver failure (Figure 6F).

Five out of six carrier-treated animals showed subdued behavior starting 24 h after surgery and subsequently fell into coma, necessitating euthanization. In stark contrast, 4 out of 6 HRX215-treated animals (pre-surgery treatment group) and 5 out of 6 animals (post-surgery treatment group) showed normal behavior and survived (Figure 6G). When analyzing explanted livers at death or intended harvesting time points, HRX215-treated livers showed normal color and texture, whereas vehicle-treated livers were smaller and appeared pale and yellowish and were underperfused (Figure 6H). In conclusion, these data suggest that the HRX215-mediated boost of liver regeneration effectively prevented a lethal PHLF upon 85% hepatectomy in pigs.

Investigational new drug (IND)-enabling Good Laboratory Practice (GLP) studies with HRX215 demonstrated the absence of any effect on the cardiovascular, neurological, or respiratory system, and in 4-week toxicity studies in rodents and non-rodents, no drug-related toxicity was observed with no observed adverse effect levels (NOAELs) of 300 mg/kg/day in rats and 250 mg/kg/day in dogs (Figure S7A). To assess the safety, tolerability, and pharmacokinetics of HRX215, a placebo-controlled exploratory phase I first-in-human study (European Union Drug Regulating Authorities Clinical Trials [EudraCT] 2021–000193-28) was performed with 48 male healthy volunteers, allocated to six treatment

groups (Figures 7A and 7B) (see STAR Methods for detailed description of the study design). In brief, no severe or serious adverse events were reported, and the number of mild to moderate adverse effects was comparable between the HRX215 and the placebo groups (13/36, 36.1% vs. 5/12, 41.7%) (Figure S7B). Complete blood counts showed no significant differences between the HRX215-treated and placebo groups (Figures S7C–S7M).

A validated liquid chromatography-tandem mass spectrometry (LC-MS/MS) method was used to investigate pharmacokinetics of HRX215 and revealed that HRX215 was rapidly absorbed, and after reaching maximum concentrations, elimination followed a biphasic manner (Figures 7C and 7D). The exposure, characterized by C_{max} and area under the curve (AUC), increased proportionally with ascending doses. When the drug was given after intake of a meal, the absorption was delayed (mean T_{max} 1.2 vs. 3.9 h), but the bioavailability of HRX215 was substantially higher (C_{max}: 1.76-fold, AUC: 2.09-fold) (Figures 7C and 7D). Overall, favorable pharmacokinetics and safety of HRX215 were observed, enabling future phase II efficacy studies.

DISCUSSION

We here describe the discovery, NMR-enabled development, and preclinical characterization of first-in-class small-molecule-based MKK4 inhibitors. Compared with small interfering RNAs (siRNAs), antisense oligonucleotides, or GalNac-conjugated oligodeoxynucleotides, small molecule inhibitors offer the advantage that therapeutic efficacy starts quickly; therefore, acute disease situations can be treated.

MKK4 inhibition increased hepatocyte proliferation and liver regeneration upon hepatectomy in murine and porcine models and also revealed antisteatotic efficacy (mouse models of ASH and NASH), as well as antifibrotic efficacy in a CCl_4 liver damage mouse model. We are convinced that the observed antisteatotic and antifibrotic activity provides a very good basis for further testing of HRX215 in chronic liver disease. However, it must be emphasized that in this context combination therapies will be necessary because HRX215 does not harbor an anti-inflammatory activity.

Unique features of HRX215 are its strong pro-regenerative effect, the underlying mechanism of action, and the excellent safety profile even after long-term treatment of HRX215. This opens up the possibility of addressing different “high medical need indications,” in which a lack of liver regeneration can result in liver failure and death of the patients, e.g., PHLF after liver resection or small-for-size syndrome after liver transplantation of small grafts. Because treatment with HRX215 prevented PHLF and allowed for survival of pigs in a lethal 85% hepatectomy model, we hypothesize that boosted liver regeneration by HRX215 might represent a viable treatment option for human PHLF. In both, patients with primary liver tumors and patients with liver metastases from colorectal cancer, the possibility of a curative therapeutic approach depends on whether the liver tumors can be completely removed. Of the approximately 1 million patients diagnosed worldwide with colorectal cancer liver metastases each year,[43] only 45% can be resected with current methodology. In the other 55% of cases, remaining functional liver volume after resection would be too low and thus put the patient at high risk for PHLF.[44] We envision that HRX215 harbors

the potential to push the boundaries of oncological liver surgery. Perioperative HRX215 treatment holds the promise to safely prevent PHLF after liver resections and will make more extensive resections possible, thus allowing a potential curative perspective for more patients with colorectal cancer liver metastases and also for patients suffering from primary liver carcinomas.

Along the same lines, we believe that HRX215 might be transformative in the field of liver transplantation, where the shortage of organs from deceased donors results in a situation in which only 10% of all patients in need for a liver transplantation can receive one.[1] Living donor liver transplantation could solve the problem, but the left lobe of the liver, which can be removed from a healthy donor at low risk, is often too small for normalsized recipients and would thus put them at risk for a "small-for-size syndrome." Owing to the HRX215-mediated rapid boost of liver regeneration, we believe that HRX215 treatment will allow for a safe transplantation of small left liver lobe grafts into normal size adults and thus will help to overcome the major problem of organ shortage in the liver transplantation field.

Limitations of the study

The liver regeneration studies presented herein were carried out in mouse and pig models, both of which are considered to be predictive of liver regeneration in humans. In particular, liver regeneration after hepatectomy in pigs seems to reflect the situation in humans after hepatectomy very well.[41] Nevertheless, the ultimate value of our therapy for increasing liver regeneration in humans will only become apparent in clinical trials. Our study includes a large number of preclinical investigations and data from a phase I study to assess the potential toxicity of pharmacological MKK4 inhibition in humans. All data indicate excellent tolerability and safety, but long-term administration should be tested in appropriate clinical trials.

STAR★METHODS

RESOURCE AVAILABILITY

Lead contact—Further information and requests for resources and reagents should be directed to and will be fulfilled by the lead contact Dr. Lars Zender (Lars.Zender@med.uni-tuebingen.de).

Materials availability—Plasmids pCaggs-FAH-IRES-GFP-shNC and pCaggs-FAH-IRES-GFP-shMKK4 are available from the Zender lab, Medical Oncology and Pneumology, Otfried-Müller Straße 14, 72076 Tübingen. A standard pET22b+ plasmid and further constructs used in the NMR study for protein expression are available from ZoBio B.V, Leiden, Netherlands.

Murine HCC cell lines *Nras*^{G12V};*Cdkn2a*$^{ARF-/-}$ and *Nras*^{G12V};*Trp53*$^{-/-}$ HCC are available from the Zender lab, Medical Oncology and Pneumology, Otfried-Müller Straße 14, 72076 Tübingen. Mouse lines pCaggs-rtTA3, TRE-GFP-shNC and TRE-GFP-shMKK4 used in this study are available from the Zender lab. FAH knockout mice have been generated by Dr. Markus Grompe[13] (Oregon Health Sciences University) and were obtained in a C57BL/6 background from Dr. Arndt Vogel (Hannover Medical School).

Data and Code availability

- mRNA data will be deposited at ENA: PRJEB72069, https://www.ebi.ac.uk/ena/browser/view/PRJEB72069 and are publicly available as of the date of publication. The unique identifier is listed in the key resources table.
- Metabolomics data will be deposited at MetaboLights[45]: MTBLS9434, www.ebi.ac.uk/metabolights/MTBLS9434 and are publicly available as of the date of publication. The unique identifier is listed in the key resources table. This paper does not report original code.
- Any additional information required to reanalyze the data reported in this paper is available from the lead contact upon request.

EXPERIMENTAL MODEL AND STUDY PARTICIPANT DETAILS

Bacteria—*E. coli* BL21(D3) cells cultured in H_2O or D_2O based M9+ medium[46] were used in this study for protein production.

Insect cells—Sf9 insect cells were cultured under standard conditions at ZoBio B.V. and used in this study for protein production.

Cell lines—Murine *Nras*^{G12V};*Cdkn2a*$^{ARF-/-}$ and *Nras*^{G12V};*Trp53*$^{-/-}$ HCC cells, overexpressing an Nras mutant (substitution of Glycin to Valin amino acid at position 12) and a deficiency of the *Cdkn2a*^{ARF} gene[39] or the *Trp53* gene, were used in our experiments. Cell lines were tested as mycoplasma negative. *Nras*^{G12V};*Cdkn2a*$^{ARF-/-}$ and *Nras*^{G12V};*Trp53*$^{-/-}$ HCC cells were cultured in DMEM supplemented with 10% fetal bovine serum, 2 mM L-glutamine, and 1% penicillin-streptomycin.

Mammalian HEK-293 cells were cultured under standard conditions at ZoBio B.V., Leiden, and used for protein production. HEK-293 cells were also used for cardiovascular safety experiments (bSys, Witterswill).

Mice—All mice experiments have been approved by the German (Animal protocols: M10_17,M3_18 and M12_19G, Tuebingen; Pharmacelsus GmbH, Saarbrücken), French (Physiogenex, Escalquenx), Danish (Gubra, Copenhagen), or Singaporian (A-star institute, Singapore) legal authorities. All mice were maintained and housed under pathogen free conditions in compliance with the institutional guidelines. Mouse strains (*Mus musculus*) utilized for experiments in Tuebingen were either bred in our in-house husbandry or were purchased from Charles River (C57BL/6 wildtype mice). The mouse strains B6.129S4-Tg(Col1AMAP2K4.3278)1MRS and B6N.FVB(Cg)-Tg(CAG-rtTA394288Slowe/J and TRE GFP shRen.713 (B6.129S4-Tg(Col1A-REN.713)1MRS were generated by Mirimus and were cross-bred in our in-house husbandry. FAH$^{-/-}$ (B6.Fahtm1Mgo) mice were generated by and obtained from Markus Grompe.[47] The A-star institute, Gubra, Physiogenex and Pharmacelsus used C57BL/6 wildtype mice for their experiments. For all mouse experiments 4–12 weeks old male and female mice were used according to the approved animal protocols.

Rats—For investigational new drug (IND)-enabling GLP studies with HRX215 8–10 weeks old female and male rats were used for the experiments according to the approved protocol. All studies were conducted in compliance with the OECD principles of Good Laboratory Practice and in compliance with animal health regulations, in particular:

Council Directive No. 2010/63/EU of 22 September 2010 and French decree No. 2013-118 of 01 February 2013 on the protection of animals used for scientific purposes.

Dogs—For investigational new drug (IND)-enabling GLP studies with HRX215 7–46 months old female and male beagle dogs were used for the experiments according to the approved protocol. Studies were conducted in compliance with the OECD principles of Good Laboratory Practice and in compliance with animal health regulations, in particular:

Council Directive No. 2010/63/EU of 22 September 2010 and French decree No. 2013-118 of 01 February 2013 on the protection of animals used for scientific purposes.

Pigs—All pig experiments have been approved by the US (Mayo Clinic) legal authorities. All pigs were maintained and housed under pathogen free conditions in compliance with the institutional guidelines. Female pigs aged between 8 and 11 weeks were used for the studies.

Human subjects—Healthy donor buffy coats were obtained from the Center for Clinical Transfusion Medicine Tuebingen (ZKT) (Blood Bank, University Hospital Tuebingen). Peripheral blood mononuclear cells were isolated from provided buffycoats and used in further experiments.

In the exploratory, double-blind, randomized, placebo-controlled trial (EUDRA-CT No. 2021-000193-28), 48 healthy male volunteers (no restrictions regarding ancestry, race and ethnicity) between 18–45 years of age were enrolled. All participants had given written and dated informed consent prior to randomization. The trial assessed safety, tolerability, and pharmacokinetics of HRX215 after single and repeated dosing under fasting and fed conditions. The phase I study was approved by the BfArM (Bundesinstitut für Arzneimittel und Medizinprodukte) and the responsible Berlin ethics committee (DE/EKBE14).

METHOD DETAILS

Cascade assay—In the cascade assay, 1 μM purified non-phosphorylated full-length MKK4 protein (ProQinase), which is unable to catalyze the phosphorylation of downstream substrates such as JNK1, was incubated with 50 nM active MEKK2 (MAP3K2, a kinase upstream of MKK4 in the stress activated protein kinase signaling pathway) (molar ratio: 20:1) in the presence of compound or vehicle and 20 μM ATP for 30 min at 30° C. Control reactions without MEKK2 confirmed the absence of MKK4 autophosphorylation. Subsequently this “activation mix” was subjected to a 100-fold dilution and MKK4 activity was determined by addition of the MKK4 substrate JNK1 KRKR. Analysis of JNK1 KRKR phosphorylation was realized by scintillation counting. The assay was optimized to quantify the inhibition of MKK4 activation within a large dynamic range, which allowed for a reliable quantification of IC50 values between the low nM and high μM concentration range.

NMR structural biology analyses—NMR structural biology analyses were conducted at ZoBio B.V. according to established protocols and are described in the following.

Construct Design—The main protein construct used for NMR resonance assignments and structure determination consisted of residues 80–399 of MKK4 (Uniprot entry: P45985) connected with a short linker (TPSSPMYVD) to a C-terminal His_6-tag for purification purposes, and C379A/C382A mutations to improve protein stability and yield. The construct was integrated into pET22b+ plasmid for expression in *E. coli*. To aid the resonance assignment process, the following 13 single mutants of MILV residues were produced, based on the NMR construct: I108L, V116I, M178L, L180I, L236I, I133L, V162I, M181L, I176L, M388L, L385I, M153L and M119L. Genes were synthesized and purchased from GenScript (Nanjing, China).

Protein Production—Protein constructs designed for resonance assignments and structure determination were expressed in *E. coli* BL21(D3) cells using H O or D 15 2 2O based M9+ medium.[46] NH_4Cl was used for ^{15}N isotope labelling. Selective labelling of ILV[48,49] and M amino acid side-chain methyl groups was achieved by adding 2-Ketobutyric acid-$^{13}C_4$,3,3-d_2 sodium salt hydrate (50 mg/l), 2-Keto-3-(methyl-d_3)-butyric acid-1,2,3,4-$^{13}C_4$,3-d sodium salt (100 mg/l) and 50 mg/l L-Methionine-2,3,3,4,4-d_5, methyl-$^{13}CH_3$. Cells were grown in shaker flasks at 37 °C (200 ml culture volume). Protein expression was induced at OD_{600} of 1.8 with 0.1 mM IPTG and protein was expressed overnight reducing the temperature to 18 °C. Cells were harvested by centrifugation; and lysed using a high-pressure homogenizer (lysis buffer: 25 mM Tris pH7.6, 250 mM NaCl, 5 mM BME, 5% glycerol, with cOmplete EDTA-free protease inhibitor tablet from Roche). The lysate was clarified by ultra-centrifugation before a standard gradient IMAC purification (0–150 mM imidazole over 40 CV) was performed using a 1 ml HiTrap TALON column (Cytiva). Fractions containing the protein of interest were pooled and concentrated using Amicon centrifugal filters, 10K MWCO (Merck Millipore) to a final concentration of 100–600 μM. Final NMR samples were prepared by exchanging the buffer to 20 mM d_{11}-Tris pH 7.4, 100 mM NaCl, 10 mM d_{10}-DTT, 4 mM $MgCl_2$, 1.25% deuterated glycerol in 5% D_2O/95% H_2O or 100% D_2O using 2 ml-ZebaSpin columns, 7K MWCO (Thermo Scientific). LN3162 was added in equimolar amounts from a 100 mM d6-DMSO stock.

NMR spectroscopy—NMR measurements were acquired on an 850 MHz Bruker Avance III HD spectrometer equipped with a 5mm TCI cryoprobe with z-gradients, or a 900 MHz Bruker Avance III spectrometer equipped with a 5 mM TCI cryoprobe with z-gradients. All samples aimed at collecting structural restraints were measured in a 5mM Shigemi tubes.

The following NMR spectra were collected on ^{2}H,^{13}C,^{15}N-labeled MILV-^{13}CH3 labeled MKK4 bound to LN3162 either in 5% D_2O/s95% H_2O and/or 100% D_2O at 298K: 2D ω2-^{13}C,^{15}N-filtered NOESY, 3D [h]CCH-NOESY[50–53] with 100 ms and 300 ms NOE mixing time, 3D ^{13}C-HMQC-NOESY[54] with 100 ms and 300 ms NOE mixing time to obtain protein-protein and protein-ligand NOEs. Through-bond CH3CG and CH3[cg]CB experiments[55] were collected to connect the pairs of methyl resonances of Val and Leu residues. 2D SOFAST-^{13}C-HMQC[56] spectra were collected for the MILV mutants. Judging

from the ^{15}N-TROSY and ^{13}C-HSQC spectra, the sample remained stable for the duration of the experiments.

Resonance assignments—In an iterative process, FLYA resonance assignment software (part of the software package CYANA,[57,58] in combination with manual inspection and information from the MILV-mutant spectra, was used to obtain assignments for almost all methyl groups involved in intermolecular NOEs.

Complex structure determination—NOE based structure calculations were performed using the 'regularize' function of CYANA with the assigned protein ligand NOE restraints added to place the ligand. Since the methyl-methyl NOEs are insufficient to define the protein part of the complex denovo, the known MKK4 crystal structures (3ALN, 3ALO and 3VUT), as well as the vemurafenib bound structures of the homologous kinases BRAF and ZAK (pdb codes: 3OG7, 4RZV, 5HES) were used as templates. These other complexes are important to include since there appears to be a specific conformation of the DFG loop induced by vemurafenib binding that we expect to be similar in MKK4 binding to LN3162. The structures were calculated from the NOEs in an iterative manner, using spin diffusion correction and recalibration based on intermediate structures to obtain more accurate restraint distances. A final set of structures was selected by taking the structure with the best NOE R-factor for each template. The NOE R-factor used here is defined as the root mean square deviation of $(NOE_{calc}/NOE_{obs})^{1/6}$.

In order to test the stability of the observed binding mode and to explore potential interactions of the ligand with solvent water molecules short (5–10 ns) MD simulations in explicit solvent, both with and without NOE distance restraints, were performed using the software GROMACS.[59]

KinomeScan—The kinase activities of the compounds of the invention were measured using KINOMEscan™ Profiling Service at DiscoveRx Corporation, 42501 Albrae St. Fremont, CA 94538, USA, which is based on a competition binding assay that quantitatively measures the ability of a compound to compete with an immobilized, active-site directed ligand. The assay was performed by combining three components: DNA-tagged kinase; immobilized ligand; and a test compound. The ability of the test compound to compete with the immobilized ligand was measured via quantitative PCR of the DNA tag. The assay was performed in the following way:

Kinases were produced in HEK-293 cells and subsequently tagged with DNA for qPCR detection. Streptavidin-coated magnetic beads were treated with biotinylated small molecule ligands for 30 minutes at room temperature to generate affinity resins for kinase assays. The liganded beads were blocked with excess biotin and washed with blocking buffer (SEABLOCK™ (Pierce), 1% BSA, 0.05% TWEEN®20, 1 mM DTT) to remove unbound ligand and to reduce nonspecific binding. Binding reactions were assembled by combining kinases, liganded affinity beads, and test compounds in 1x binding buffer (20% SEABLOCK™, 0.17x PBS, 0.05% TWEEN®20, 6 mM DTT). All reactions were performed in polystyrene 96-well plates in a final volume of 0.135 ml. The assay plates were incubated at room temperature with shaking for 1 hour and the affinity beads were washed with wash

buffer (1x PBS, 0.05% TWEEN®20). The beads were then re-suspended in elution buffer (1x PBS, 0.05% TWEEN®20, 0.5 11 M non-biotinylated affinity ligand) and incubated at room temperature with shaking for 30 minutes. The kinase concentration in the eluates was measured by qPCR.[60,61]

Average Z' values and standard deviations were calculated for each kinase based on fourteen control wells per experiment in over 135 independent experiments spanning a period of sixteen months. Average Z' = 0.71.

MKK4 binding and selectivity assay—MKK4 inhibitors were profiled in a radiometric protein kinase assay (^{33}PanQinase® Activity Assay) by ProQinase (Reaction Biology) according to their protocols. In short, the assay for all protein kinases contained 70 mM HEPES-NaOH pH 7.5, 3 mM $MgCl_2$, 3 mM $MnCl_2$, 3 μM Na orthovanadate, 1.2 mM DTT, 50 μg/ml PEG20000, ATP (variable concentrations, corresponding to the apparent ATP-Km of the respective kinase), [γ−^{33}P]-ATP (approx. 9 × 10^05 cpm per well), protein kinase and substrate. Incorporation of ^{33}Pi was determined with a microplate scintillation counter (Microbeta, Wallac). IC_{50} values of MKK4 inhibitors were measured in singlicates by screening 10 distinct concentrations in a semi-logarithmic dilution series (1*10^−04 M to 3*10^−09 M) on different protein kinases (MKK4: 4.1 nM, MKK7: 45.4 nM, JNK1: 2.3 nM, $BRAF^{wt}$: 14.5 nM). All protein kinases provided by ProQinase were expressed in Sf9 insect cells or in *E. coli* as recombinant GST-fusion proteins or His-tagged proteins, either as full-length or enzymatically active fragments. Affinity tags were removed from a number of kinases during purification. The purity of the protein kinases was examined by SDS-PAGE/Coomassie staining, the identity was checked by mass spectroscopy.

Immunoblotting—Isolated proteins were transferred via a semi dry blot system (Trans blot SD Semi Dry transfer cell, Bio Rad) or a wet-transfer system on Nitrocellulose or Immobilon-P membranes (Millipore) in transfer buffer with 15 to 20V for 30 min (semi-dry system) or 100 to 130 V for 2 h (wet-transfer system). Blocking of membranes were performed with 5 % BSA (Roth) or 5 % milk in TBST (for p-antibodies). The membranes were incubated with the primary antibodies against alpha-Tubulin (CST2125; 1:1000), Vinculin (V9131; 1:15000), MKK4 (CST9152; 1:1000), p-MKK4 (S257) (CST4514; 1:1000), p-MKK7 (S271/Y275) (*bs*-3277R; 1:1000), p-JNK1/2 (T183/Y185) (CST4688; 1:1000), p-p38 (T180/Y182) (CST4511; 1:1000), p-ATF2 (T69 or 51) (ab131106), p-ATF2 (T71) (ab32019; 1:1000), p-Elk1 (S383) (CST9181; 1:1000); p-IκB alpha (S32) (CST2859; 1:1000); p-NFκB-p65 (S276) (GTX54672; 1:1000); p-p53 (S46) (CST2521; 1:1000); Bcl-XL (CST2764; 1:1000); Cdc25C (CST4688; 1:1000), CDK4 (ab137675; 1:1000), Cyclin A2 (ab38; 1:1000), Cyclin B1 (CST4138; 1:1000), Cyclin E1 (CST20808; 1:1000); Cyclin D1 (CST2922; 1:1000); Stathmin (CST13655; 1:1000); EGFR (CST2232; 1:1000); HER2/ErbB2 (CST4290; 1:1000); p-ERK1/2 (T202/Y204) (CST9101; 1:1000) in the blocking solution or TBST with 5% BSA or milk at 4 °C overnight or at room temperature for 1 hour. Washing of membranes was performed three times with PBST or TBST for each 10 minutes. Afterwards membranes were incubated with the corresponding secondary antibody (1:5000) at room temperature for 1 hour in PBST or TBST. After washing, the blots were

visualized in the ChemiDocTM MP Imaging System (Bio-Rad) using Lumi-light Western Blotting Substrate (Roche). Membranes were analyzed via the software Image Lab 4.1.

Target engagement assay—PBMCs were isolated from prepared buffycoats in a standard Ficoll gradient procedure to develop a target engagement assay for MKK4. Isolated PBMCs were preincubated with 0.3, 1 and 3 μM HRX215 in RPMI (1% P/S, 10% FCS) at 37° C for 2 hours. Afterwards activation of the MAPK signaling pathway was induced by the addition of 1 μg/ml LPS for 1 h. Harvested cells were lysed with NP-40 Buffer (50 μM TrisHCl, pH7.4, 150 mM NaCl, 0.5% NP-40 including protease and phosphatase inhibitors) and total protein concentrations were determined according to the DC Protein Assay Instruction Manual.

The following immunoblotting was performed as described above with an anti-p-MKK4 (S257) antibody (CST4514). A ChemiDoc MP Imaging System was used to visualize p-MKK4 levels. Intensity of protein bands were quantified via ImageJ and analyzed in GraphPad Prism.

Trypan blue staining—Adherent *Nras*^{G12V};*Cdkn2a*$^{ARF-/-}$ and *Nras*^{G12V};*Trp53*$^{-/-}$ HCC cells treated either with DMSO or HRX215 10 μM were collected and mixed with Trypan blue solution in a ratio of 1:2. Total and stained cells were counted in a Neubauer chamber to calculate percentage of death cells.

Crystal violet staining—Adherent *Nras*^{G12V};*Cdkn2a*$^{ARF-/-}$ and *Nras*^{G12V};*Trp53*$^{-/-}$ HCC cells treated either with DMSO or HRX215 10 μM for 3 days were washed with PBS once and fixed with 10% formaldehyde solution in cell culture plates for 20 min. After 2 washing steps with MilliQ, fixed cells were stained with 0.1% crystal violet solution for 15 min followed by washing with MilliQ. The plates were air-dried and scanned with a Lexmark CX510de.

In vivo MKK4 knockdown analyses—The mouse strains pCaggs-rtTA3 x TRE GFP shRen.713 and rtTA3 x TRE GFP shMAP2K4.3278 were bred in an in-house husbandry in Tuebingen. Male and female mice aged around 12 weeks were set on dox food for 3–5 days to activate shRNA expression. At the endpoint, mice and organs were imaged for fluorescence GFP expression utilizing the Hamamatsu Imaging system as described previously.[4] Tissues were screened for MKK4 knockdown via immunoblotting.

Partial Hepatectomy of shRNA transgenic mice—The mouse strains pCaggs-rtTA3 x TRE GFP shRen.713 and rtTA3 x TRE GFP shMAP2K4.3278 were bred in an in-house husbandry in Tuebingen. Before PH, around 12-weeks old mice (male or female) were set on dox food for 3 days to activate shRNA expression. PH was conducted according to standard protocol[62] with minor modifications. Livers were harvested after 48 h, paraffin embedded and analyzed for Ki67 in immunofluorescence stainings.

Long-term MKK4 knockdown in mice—The mouse strains pCaggs-rtTA3 x TRE GFP shRen.713 and rtTA3 x TRE GFP shMAP2K4.3278 were bred in an in-house husbandry in Tuebingen. Around 12-weeks old mice (male) were fed with dox food for 12 months.

Weight was constantly measured, tissues were collected and fixed with 4% PFA at the end of the experiment. H&E stainings were analyzed by a board-certified pathologist (T.L.).

Long-term MKK4 knockdown in a NASH-HCC model—$FAH^{-/-}$ mice were kept on NTBC after birth for 4 weeks. To induce liver repopulation $FAH^{-/-}$ mice (male) were transfected via HDTV with an SB13 construct as well as a construct carrying the full length *Fah* gene and either an shRNA against Renilla (control) or MKK4 (CAG-FAH-IRES-GFP-shRNA-pA). 24 hours after HDTV, NTBC was removed to start repopulation of the liver for 60 days. Eight weeks after *in vivo* delivery of transposon vectors via hydrodynamic injection full liver repopulation was accomplished. After complete liver repopulation mice were fed with choline-deficient high fat diet (CD-HFD) over 42 weeks. Survival of the mice was recorded and livers were collected for further analysis.

Pharmacokinetics—Blood concentrations of HRX215 in around 8 weeks old C57BL/6 wildtype mice (male) were measured by Pharmacelsus GmbH according to standard procedures. In each case, HRX215 was administered p.o. in a vehicle of 0.5% HPMC in 0.1 M K_2HPO_4 in a single dose of 30 mg/kg to 3 mice and blood samples were taken at 15 min, 30 min, 1 h, 2 h, 3 h, 8 h and 24 h after administration of the test item. All samples were stored at −20°C until LC-MS analysis. The pharmacokinetic analysis was performed by applying a non-compartment model using the Kinetica 5.0 software (Thermo Scientific, Waltham, USA). All given parameters were obtained by trapezoid area calculation.

Partial hepatectomy in wildtype mice—PH was either conducted at Gubra (Denmark) or at the Biological Resource Centre *BRC A*STAR (Singapore) according to standard protocols[62] with minor modifications. Ventral lobes were clamped with a suture to impair bleeding before resecting PH of the liver. C57BL/6 wildtype mice were 6–12 weeks old at the start of PH. Before PH on mouse livers, wildtype mice (male and female) were either treated with vehicle or HRX215 (0.4, 2 or 10 mg/kg) 8–12 and 1 hour via p.o. prior to partial hepatectomy. Livers were either snap-frozen, embedded in Tissue-Tek OCT or fixed in 4% PFA for paraffin embedding at timepoint 0h, 1h, 42h or 48h for further analysis. Used mice for PH were either untreated wildtype mice or wildtype mice treated with CCl_4 (0.25 ml/kg in sunflower oil; i.p.; twice per week) for 3 weeks.

Short-term CCl_4 liver damage model—The short-term CCl_4 liver damage model was conducted at Physiogenex. Around 8 weeks old C57BL/6 wildtype mice (male) were treated with vehicle or HRX215 (0.4, 2 or 10 mg/kg) 12 and 1 hour prior to liver damage induction via one-dose CCl_4 (0.25 ml/kg in sunflower oil; i.p.). A third dose vehicle or HRX215 (0.4, 2 or 10 mg/kg) was administered 24 hours after CCl_4 treatment. Liver tissue was collected 48 hours after CCl_4 treatment and used for further analysis.

Lieber-DeCarli (ASH) model—C57BL6 wildtype mice (female) aged 8–12 weeks were treated with Lieber-DeCarli diet and binge[63] in an acute-on-chronic liver damage model. Mice were fed with Lieber-DeCarli diet in increasing concentrations of Lieber-DeCarli diet with Alcohol. Lieber-DeCarli diet was prepared freshly on a daily basis. After 5 days of increasing alcohol concentration in the food mixing Control Lieber-DeCarli diet and Ethanol Lieber-DeCarli diet, mice were fed with 100% Ethanol Lieber-DeCarli diet

prepared according to manufactures instructions (Rodent Liquid Diet Lieber-DeCarli'82 Control (F1259) and Rodent Liquid diet Lieber-DeCarli'82 Ethanol (F1258), Bio Serv US and Canada). Treatment was done at the same time of the day. Food was freshly prepared in the evening on a daily basis and provided in excess with 10 ml liquid food per mouse. At day 10 the animals received an additional binge of 5 g/kg alcohol in a 35% Ethanol /water solution. HRX215 (0.4, 2, 10 mg/kg) or vehicle was daily administered via p.o. over 5 days before euthanization of mice. Mice livers were collected and analyzed after 15 days.

Long-term CCl_4 model—CCl_4 was dissolved in sunflower oil in a ratio 1:20. 5 μl/g of the mixture was administered to around 12 weeks old C57BL/6 wildtype mice (female) via i.p. to reach a final concentration of 0.25 μl/g CCl_4. Mice were treated for 6 weeks twice a week to induce fibrosis. 3 weeks after initial start of CCl_4 injections, mice were additionally treated with MKK4i 10 mg/kg (twice per day; p.o.) for another 3 weeks. After 6 weeks mice livers were collected and analyzed.

4-week toxicity study in wildtype mice—C57BL/6 wildtype mice (female) aged 8–12 weeks were daily treated with HRX215 (10 mg/kg) or vehicle via p.o. over 4 weeks. Plasma and livers were collected at the endpoint and further analyzed.

Short-term GAN NASH and long-term GAN NASH HCC model—C57Bl/6 wildtype mice (male) aged around 5–6 weeks were fed with Gubra Amylin NASH (GAN) diet which is based on a 40% high fat diet (for DIO-NASH model) for 38 weeks in a model to evaluate the NAFLD score or for 64 weeks in a NASH dependent tumor model prior to start with a daily HRX215 (10 mg/kg) or vehicle treatment at Gubra (Denmark) over 12 weeks. Study inclusion criteria for all animals in a steatotic mouse model were based on the histological conformation of steatosis score ≥2 and fibrosis stage =3 from a pre-study liver biopsy. 20 animals fulfilling those criteria were sacrificed for a baseline of tumor burden (tumors/liver and tumor volume). After 12 weeks of treatment 20 mice in the vehicle group and 19 mice in the HRX-215 (10 mg/kg) group were sacrificed and analyzed regarding NAFLD score, tumor number per liver and tumor volume.

In vivo formulation of MKK4i—For preparation of the formulation, a 0.5% (w/v) HPMC solution was prepared. For a 1 mg/ml solution 20 mg of MKK4i is suspended in 1 ml 0.5% (w/v) HPMC $solution_{aq}$ and ground with a spatula. The remaining 19 ml 0.5% (w/v) HPMC $solution_{aq}$ were added and stirred with a spatula. The sample is suspended by vortexing for min. 30 sec followed by sonication for min. 3 min. Afterwards aliquots for daily supply were prepared and stored at −20°C for 7 days. Immediately before administration, aliquots should be thawed and vortexed for 30 s to obtain a homogenous suspension before administration to the animals.

Apoptosis phosphoprotein antibody array—Whole cell lysates of *Nras p19*$^{Arf-/-}$ HCC cells and liver tissues were used in the ELISA-based apoptosis phospho antibody array (Full Moon Biosystems, Inc.) according to their user guidelines. In short, lysates were centrifuged at 18,000 × g for 20 minutes to clear lysates and the supernatant is transferred to a new reaction tube. In the next step, buffer of the protein lysates was exchanged replaced with the labeling buffer. Lysates were quantified via UV absorbance and afterwards around

100 μg of protein was biotinylated following by a blocking step of the samples. Samples were extensively washed with MilliQ, coupled with the coupling solution and again washed with MilliQ. IRDye 800CW Streptavidin (1:1000) was used to detect biotinylated proteins on an LI-COR Odyssey imager. Images were analysed in the LI-COR image studio software. Anaylsis was performed according to Wuestefeld et al.[4] and Kang et al.[64] Dendrogram and hierarical clustering was performed with the web tool heatmapper.

RNA Sequencing—RNA Sequencing was conducted with CeGaT GmbH according to their protocols. RNA isolation from cell pellets and tissue samples were performed with MagMAX™ mirVana™ Total RNA Isolation Kit (Thermo Fischer Scientific) which was automatized on a KingFisher Flex instrument (Thermo Fischer Scientific).

For RNA-library preparation with a TruSeq Stranded mRNA kit (Illumina) 100 ng of mRNA were used and afterwards sequenced on a NovaSeq 6000 system (Illumina). The sequencing reads were demultiplexed with Illumina bcl2 fastq (2.20). Adapters were trimmed with Skewer (version 0.2.2).[65] A quality trimming of the reads has not been conducted. Trimmed raw reads were aligned to mm10 using STAR (version 2.7.3).[66]

Differential expression analysis between groups was performed with DESeq2 (version 1.24.0)[67] in R (version 4.0.4).[68] DESeq2 uses a negative binomial generalized linear model to test for differential expression based on gene counts. The raw counts derived from the mapping contained the number of reads that map to each geneID. Based on these numbers the normalized counts were calculated. In the first step of the normalization DESeq2 calculated a fictive “reference sample” which is defined as the geometric mean for each gene across all samples regardless of group affiliation. The counts for each gene and sample were then divided by this reference value. In the next step the size factor was estimated for each sample by calculating the median of these ratios. To get the normalized counts, for each gene and sample the raw counts were divided by the sample’s size factor. This normalization accounts for different library sizes and for biases if, e.g., in some samples only a few genes are very highly expressed.

As recommended by DESeq2, we removed genes with less than two reads over all samples. This improves the detection power by making the multiple testing adjustment of the p-values less severe. Using normalized counts DESeq2 calculated the $\log_2$ fold change, where the p-value reports the statistical significance of this result (Wald test). To correct for multiple testing, we used the Benjamini-Hochberg correction[69] implemented in DESeq2 to adjust the p-value (padj). Hence, the padj value should be used to determine significant differences in gene expression.

Average of normalized counts (21563 genes) between the shMKK4 and HRX215 group were analyzed in an expression correlation. Cut-off criteria of significant gene expression changes between the groups: log2fold change>2 (Foldchange4/−4), p-adjust<0.01, average expression level≥100. Both axes were logarithmized (basis 2) and the correlation coefficient and p-value were calculated.

Untargeted metabolomic profiling—Metabolite extraction from liver tissue and untargeted metabolomic profiling was done as described.[70,71] In brief, frozen tissue samples of approximately 20–40 mg (NASH mouse: n=18 vehicle, n=18 MKK4i 10 mg/kg) and 40–120 mg (WT mouse: n=4 vehicle, n=4 MKK4i 10 mg/kg) were randomised for each sample set. Samples were homogenized by bead beating followed by two-step metabolite extraction at solvent/tissue ratios of 25 µl/mg (NASH mouse) and 10 µl/mg (WT mouse), respectively. 50 µl of the supernatants were transferred to a new vial and dried at 40° C under a gentle nitrogen stream. Dried aqueous extracts were reconstituted in water/acetonitrile (5:95, v/v) to a final concentration of 0.01 mg/µl. Quality control (QC) samples were prepared for each batch by pooling equal volumes of reconstituted samples (i.e., one QC sample was prepared from aqueous extracts and one QC sample from organic extracts). Metabolite extracts were analyzed after hydrophilic interaction chromatography (HILIC) separation in positive and negative ionisation mode with an injection volume of 1 µl. Metabolites were extracted from plasma samples by methanol precipitation. Briefly, ice-cold methanol (120 µl) was added to 30 µl of plasma sample (NASH mouse: n=17 vehicle, n=15 MKK4i 10 mg/kg; WT mouse: n=4 vehicle, n=4 MKK4i 10 mg/kg) and vortexed for 30 s followed by incubation for 20 min at −20° C. After centrifugation (16,100g, 10 min, 4° C) 60 µl of the supernatant was transferred to a clean tube, dried and reconstituted in 60 µl water/acetonitrile (5:95, v/v). 1µl was injected and analyzed after HILIC separation in positive and negative ionization mode.

Preprocessing of non-targeted metabolomics data was performed using the Mass Hunter Profinder Software (version B.08.00, Agilent Technologies) with batch recursive feature extraction[70,72] at an intensity threshold of 500 counts. H+, Na+ and NH4+ adducts were selected for positive mode data, while the deprotonated molecular ions and CH3COO- and HCOO-adducts were expected for negative mode data. The retention time window was set to ±0.2 min, the mass window to ±(20 ppm + 2 mDa) and the extracted ion chromatogram (EIC) range to ±35 ppm. Compounds were filtered by MFE scoring, where a compound must have an MFE score >70 in at least 80% of the files in at least one sample group. The Agile2 algorithm was selected for peak integration. TOF-MS spectra were excluded if their intensity was above 30% saturation. The list of extracted features was visually inspected to ensure correct retention time alignment and peak integration throughout the batch. More specifically, the extracted ion chromatograms (EICs) of individual features and their chromatographic alignment throughout the analytical batch were checked using a graphical interface. Curations were made by manual reintegration of EICs that had been incorrectly integrated by the software algorithm (e.g. correct peak integrations of closely coeluting isomeric compounds in two different samples). The extracted features were exported as comma separated value (csv) files and used for further statistical analysis. Feature lists were sum-normalised (i.e., the peak area for each feature was divided by the sum of all features per mode) and feature lists from the different ionisation modes were merged. QC filtering (features with CV ≥25% over the QC samples were removed) and $\log_2$ transformation was then applied. Features differentially altered between MKK4i treated and vehicle control samples were assessed using linear modeling and related empirical Bayes moderated t tests.[73] Resulting P-values were adjusted for multiple testing by the Benjamini-Hochberg (BH) procedure.[69] BH-adjusted P values <0.05 were considered as significant while an absolute $\log_2$ fold change ≥1 was considered as relevant. R statistical software (version

4.2.3)[74] was used for normalisation, CV filtering and linear modeling using the additional package limma.[75,76] Volcano plots were generated using the gplot package.[77]

Structural assignment of differentially altered features was achieved using fragment mass spectra (MS/MS) acquired by automated MS/MS analysis in pooled QC samples. MS/MS spectra were analysed using Mass Hunter Qualitative Analysis software (version B.07.00, Agilent Technologies) and exported in Mascot Generic Format (MGF), followed by annotation using the SIRUS workflow.[78] Metabolites were considered as putatively annotated if they achieved a reported structure score of >70%.

Structural annotation of drug metabolites related to HRX215 was supported by analysis of pure reference substances HRX215 and HRX215-glucuronide.

Hydrodynamic injections—For hydrodynamic tail vein injection plasmid DNA was prepared with the Pure Yield Maxi Kit (Promega) including endotoxin removal buffer. The transposable element and transposase SB13 encoding plasmid DNA were mixed in a ratio 5 : 1 (25 μg: 5 μg or 1.25 μg: 0.25 μg). Mixed DNA was diluted in 0.9% NaCl solution at a final volume of 10% of the mouse weight and injected into the tail vein within 10 seconds. Hepatocytes take up the injected volume due to a transient heart failure and allows expression of genes and shRNAs. Mice were injected at 5 to 7 weeks of age.

Paraffin embedding of tissue sections—Tissues of different organs were fixed with 4% PFA in PBS up to 2 days, embedded in paraffin and cut.

Haematoxylin and eosin staining—Deparaffinized and rehydrated slides for haematoxylin and eosin (H&E) stainings were first stained with Haematoxylin for 7 min, quickly washed in H2O and blued for 20 min under running tapwater. Secondly, an eosin staining was performed for 2 min followed by a hydration procedure. Slides were mounted with Neo Lab mounting medium. White areas on H&E stained sections were used for the analysis of steatotic areas in the ASH model.

Sirius Red staining—Sirius Red staining was performed on deparaffinized and rehydrated liver sections. Sections were incubated with 0.1% Picro Sirius Red solution at room temperature for 1 h and quickly cleared in 0.5% acidified water within 3 consecutive cycles. Afterwards, samples were dehydrated with ethanol and xylol and finally mounted.

Immunohistochemistry—Paraffin embedded liver sections were deparaffinized and rehydrated on slides. Antigen retrieval was performed in Citrate buffer in a pressure cooker for 10 minutes. After washing the slides in TBS, they were exposed to 3 % H_2O_2 for 10 minutes at 4 °C and washed again. The slides were blocked with Zytomed blocking solution for 5 minutes at room temperature and washed again in TBS. Primary antibody were diluted in Antibody diluent (Zytomed) and the staining was performed at 4 °C overnight. Antibodies used in this manner: anti-Ki67, anti-p21, anti-γH2Ax and anti-alpha smooth muscle actin (SMA). Slides were again washed in TBS and incubated with secondary antibody in biotinylated secondary antibody solutions (Thermo Scientific) for 1 hour at room temperature. After another washing step, the slides were incubated with

Streptavidin-Horseradish peroxidase (HRP) conjugate antibody (Zytomed) for 10 minutes at room temperature, washed again and stained with 3,3'- Diaminobenzidine (DAB) until they were brown colored (1 to 5 min at room temperature). Slides were washed in water, counterstained with hematoxylin solution (Roth) for 30 seconds, washed in water again, dehydrated with ethanol and xylol (Roth) and mounted.

Terminal deoxynuleotidyl transferase dUTP nick end labeling—TdT-mediated dUTP-biotin nick end labeling (TUNEL) staining was either performed at Physiogenex according to their protocols or in Tuebingen. Apoptotic cells in liver tissue were stained with the TUNEL Kit (Roche) together with 1 μg/ml DAPI on either paraffin or snap frozen tissue sections.

Cryosections—Snap frozen tissue samples were embedded in Tissue-Tec OCT (Sakura, Leiden, Netherlands) and cut using a HM 560 cryostat.

Frozen tissue immunofluorescence staining—Immunofluorescence (IF) stainings were conducted with 8 μm sections derived from snap frozen tissues. Sections were fixed with 4% paraformaldehyde (in TBS) for 10 min and washed with TBS three times followed by a blocking step with normal goat serum (NGS) blocking solution. Samples were washed with TBS-T and subsequently incubated with respective primary antibodies (anti-Ki67) in TBS-T with 1% NGS at 4° C overnight. Afterwards, slides were washed with TBS-T in three cycles and incubated with a secondary antibody together with 1 μg/ml DAPI in TBS-T with 1% NGS at room temperature in the dark for 1 h. After three consecutive washing steps with TBS-T, samples were mounted with Vectashield H-1000 mounting medium.

Microscopic analysis and cell counting—Microscopic analysis and pictures were imaged with the Olympus BX63 (Olympus). Counting of immunohistochemical stainings or cell fractions was done by counting 8 to 20 optical fields using ImageJ. Stains were otherwise evaluated using the software Cognition Master Professional Suite (VM scope, Berlin Germany) by the hot spot method.

Histopathological evaluation—Histopathological evaluation of murine livers and liver tumors was done on H&E stainings by the board-certified pathologists Thomas Longerich from the University of Heidelberg and Bence Sipos from the University of Tuebingen.

Pig husbandry—All animals were obtained from a local vendor (Manthei Hog Farm, Elk River, MN) under IACUC protocol number A00003741–18. All animal husbandry and procedures were performed in accordance with the guidelines set forth by the Mayo Institutional Animal Care and Use Committee.

Intracranial pressure (ICP) probe and central venous catheter (CVC) placement—General anesthesia (induction: 5 mg/kg Telazol, and 2 mg/kg Xylazine; maintenance: inhaled isoflurane 1% 4%) was administered to all pigs. The ambulatory ICP probe (Raumedic, Germany) included an intraparenchymal catheter placed and a subcutaneous transmitter which were inserted in the pig.[79] A cuffed double-lumen central venous catheter (Palindrome 55 cm, Covidien, Mansfield, MA) was placed in the right

internal jugular vein by Seldinger technique, tunneled subcutaneously and exited from the pig's back.[79] The central line was locked with 3 ml of 4% sodium citrate per lumen daily to maintain patency. Animals were recovered and then received standard animal care for 3–7 days to allow healing of incisions and confirm health status before performing the liver resection.

Partial hepatectomy in pigs—The herein applied partial hepatectomy procedure was previously published by Croome et al.[80] and described in that study in more detail. In short, all pigs were sedated with an IM injection of Telazol (5 mg/kg) + Xylazine (2 mg/kg). The abdomen was prepped with betadine and midline laparotomy was performed from the xiphoid process to the level of the umbilicus. The Omni retractor was placed to provide adequate exposure of the liver and portal vasculature. All peritoneal attachments were released, and portal vein, hepatic artery, and hepatic veins were identified and isolated. Hepatectomy was proceeded from left to right using a clamp and crush technique. 80 and 85% hepatectomy involved the removal of the left lateral lobe and both left and right medial lobes and most of the right lateral lobe leaving the caudate lobe and the small part of the right lateral lobe as remnant liver parenchyma. Bleeding from the parenchyma was controlled with cautery or suture ligation. The cut edges of the liver parenchyma were addressed with 3–0 or 4–0 Prolene sutures to ensure hemostasis and minimize the risk for bile leak.

Abdominal CT imaging and volumetry—All pigs underwent abdominal CT imaging with arterial and portal phases immediately before and after resection and at 43 h (80% and 85% PH) and 90 hr (85% PH) time points. Intravenous contrast of 60-mL Omnipaque (GE Healthcare, Princeton, NJ) was given through a peripheral ear vein to better delineate the edges of liver parenchyma. Solumedrol 50mg IV and diphenhydramine 25 mg IV were given if the animals developed an anaphylactic reaction to the contrast. CT images were uploaded to 3D volumetric software (TeraRecon, Foster City, CA) to estimate the liver volume.[80] Standardized liver volume was calculated by the following equation: SLV = −794.41 + 1267.28 × body surface area (m^2).[80,81] All CT volumetric results were confirmed by a blinded radiologist. Volume regeneration index RI, defined as the liver volume at a specific time-point divided by the volume immediately after hepatectomy, was used as the main parameter to measure the level of regeneration in our study. RI at 43 h and 90 h timepoints were applied in all pigs.

Functional data from porcine blood samples—Blood samples during the 85% hepatectomy study were taken for evaluating the liver function tests (AST, Alanine aminotransferase (ALT), bilirubin, INR, and ammonia) at the following time points: −24 h, T0, 12 h, 24 h, 36 h, 48 h, 60 h, 72 h, 84 h, 90 h where T0 is the time of completing hepatectomy.

Investigational new drug (IND)-enabling GLP studies (4-week toxicity study in rodents and non-rodents)—The IND-enabling GLP studies were initiated by investigating cardiovascular safety. First, HRX215 at 0.667, 6.67 and 20 μM was tested on HEK293 cells that stably express the hERG (human-ether-à-go-go related gene) potassium

channel in a whole-cell patch-clamp technique. Second, 4 male beagle dogs with an age of 21–46 months received 0, 50, 125 and 250 mg/kg HRX215 p.o.. At the endpoint, mortality, clinical signs, body weights, body temperature, blood pressure (systolic, diastolic and mean arterial), heart rate and the electrocardiogram (QRS duration and the RR, PR, QT and corrected QT [QTc] intervals) were measured. To test the respiratory function 32 male Wistar Han rats (Charles River Laboratories) were used. The animals were approximately 9 weeks old when they received 0 (vehicle only), 30, 100 or 300 mg/kg HRX215 p.o.. Endpoint measurements included mortality, clinical signs and respiratory function (respiratory rate, tidal volume, and minute volume). Also, CNS function was validated in 32 male, approximately 10 weeks old, Wistar Han rats (Charles River Laboratories). The animals received 0 (vehicle only), 30, 100 or 300 mg/kg HRX215 p.o.. The following parameters and endpoints were evaluated in this study: mortality, clinical signs, and FOB evaluations.[82] Afterwards, general toxicity was evaluated in 152 Wistar Han rats (76 males and 76 females; Charles River Laboratories) and 32 beagle dogs (16 males and 16 females; Charles River Laboratories). The experiment was started with approximately 8 weeks old rats and 7–8 months old beagle dogs. Rats received 0, 30, 100 and 300 mg/kg/day HRX215 p.o. and beagle dogs were treated with 0, 100, 250 and 375 mg/kg/day HRX215 p.o.. Assessment of toxicity was based on mortality, clinical observations, body weight, food consumption, ophthalmology, standard laboratory investigations, bone marrow micronucleus analysis (only from rat samples) and histopathological evaluations (including organ weights). On completion of the treatment or treatment-free period, the animals were euthanized and a complete macroscopic *post-mortem* examination was performed. Designated organs were weighed and selected tissues were preserved. A microscopic examination was performed on selected tissues for the control and high-dose animals and on all macroscopic lesions from all low- and mid-dose animals.

First-in-human (FIH) phase I clinical trial (EUDRA-CT No. 2021-000193-28)— The primary objective of this FIH study (sponsor: HepaRegeniX GmbH) was to investigate the safety and tolerability of HRX215 after single and multiple doses. Furthermore, the pharmacokinetics of HRX215 were investigated as an exploratory endpoint. The study design followed the recommendations of the of the EU guideline on mitigation of risks in early clinical trials. The trial registered in the *EudraCT* (European Union Drug Regulating Authorities Clinical Trials) database on 13 Jan 2021 and approved from German authorities on 08 Jul 2021, was conducted in a single-center, randomized, double-blind (intra-individual), placebo-controlled design with increasing single and multiple doses in 48 healthy male subjects (age between 18 and 45 years, good physical health as determined by medical and physical examination, 12-lead ECG, vital signs and clinical laboratory tests; BMI between 18.5 and 29.9 kg/m^2; normal blood pressure and pulse rate). The first volunteer was enrolled on 22 Jul 2021. Within each dose step, 8 healthy male subjects were randomized to either HRX215 (6 subjects) or respective placebo (2 subjects). With the solid, crystalline active ingredient, a capsule formulation with two different dose strengths, 5 mg and 50 mg, was developed. In the first period, single ascending doses between 5 mg and 500 mg were administered. In period 2, volunteers of the 50 mg dose level received the same treatment, but the drug was administered after intake of a high-calorie breakfast, while subjects receiving 100 mg, 250 mg and 500 mg were recruited for a 7-day treatment

with the same dose, which was administered either twice daily (100 mg, 250 mg) or once daily (500 mg) (Figure 7A). To investigate the pharmacokinetics of HRX215, serial blood samples were taken after single dose administration, as well as on day 1 and day 7 during multiple administrations. Before escalating to the next dose level, safety and PK data were reviewed by a safety assessment team. Safety evaluation included serial 12-lead ECGs between pre-dose and 72h post dose, adverse events and vital signs recording as well as safety laboratory analyses (hematology/coagulation, clinical chemistry and urinalysis).

QUANTIFICATION AND STATISTICAL ANALYSIS

Software for experimental quantification are named in the respective methods part. Graphs and statistical test were performed in GrahPad Prism 9.4.1. Analysis of the apoptosis array, RNA sequencing and metabolomics are further described in the respective method sections. Statistical test information, statistical significance values, error bars, number of replicates and numbers of mice per group and scale bars are indicated in the figures and the figure legends.

ADDITIONAL RESOURCES

Information and data of our FIH phase I study (EUDRA-CT No. 2021-000193-28) will be deposited at Zenodo. They are publicly available as of the date of publication until 01.01.2029. Description: Zenodo (https://zenodo.org//): https://doi.org/10.5281/zenodo.10558364; also listed in the key resources table.

Supplementary Material

Refer to Web version on PubMed Central for supplementary material.

ACKNOWLEDGMENTS

We thank all members of the Zender laboratory for discussions. We thank Pearl Schiemann, Lea Herrmann, and Markus König for technical assistance and Morgana Barroso Oquendo and Sven Nahnsen for annotation and management of high-throughput data. We thank the Gubra team for conducting NASH-HCC studies and Misbha Ud Din Ahmad for conducting X-ray crystal-lography work. We thank CRS Clinical Research Services Berlin for conducting the phase I trial. We thank Hugo van Ingen (Utrecht University) and Tammo Diercks (CIC bioGUNE, Bilbao) for assistance with NMR experiments and providing pulse sequences. This work was supported by the German Research Foundation (DFG), projects: FOR2314, 267467939 (L.Z.), SFB-TR209-314905040 (L.Z.), SFB-TR240 (L.Z.), and under Germany's excellence strategy EXC 2180-390900677 (iFIT) (L.Z., S.L., and M.S.), the Gottfried Wilhelm Leibniz Program (L.Z.), the German Cancer Consortium (DKTK) (L.Z.), the Robert Bosch Stiftung (M.S.), and HepaRegeniX GmbH (S.L. and L.Z.). The phase I study was funded by HepaRegeniX GmbH.

REFERENCES

1. Asrani SK, Devarbhavi H, Eaton J, and Kamath PS (2019). Burden of liver diseases in the world. J. Hepatol 70, 151–171. [PubMed: 30266282]
2. GBD (2020). The global, regional, and national burden of cirrhosis by cause in 195 countries and territories, 1990–2017: a systematic analysis for the Global Burden of Disease Study 2017. Lancet Gastroenterol. Hepatol 5, 245–266. [PubMed: 31981519]
3. Campana L, Esser H, Huch M, and Forbes S (2021). Liver regeneration and inflammation: from fundamental science to clinical applications. Nat. Rev. Mol. Cell Biol 22, 608–624. [PubMed: 34079104]

4. Wuestefeld T, Pesic M, Rudalska R, Dauch D, Longerich T, Kang TW, Yevsa T, Heinzmann F, Hoenicke L, Hohmeyer A, et al. (2013). A Direct In Vivo RNAi Screen Identifies MKK4 as a Key Regulator of Liver Regeneration. Cell 153, 389–401. [PubMed: 23582328]
5. Canovas B, and Nebreda AR (2021). Diversity and versatility of p38 kinase signalling in health and disease. Nat. Rev. Mol. Cell Biol 22, 346–366. [PubMed: 33504982]
6. Shen YH, Godlewski J, Zhu J, Sathyanarayana P, Leaner V, Birrer MJ, Rana A, and Tzivion G (2003). Cross-talk between JNK/SAPK and ERK/MAPK Pathways: SUSTAINED ACTIVATION OF JNK BLOCKS ERK ACTIVATION BY MITOGENIC FACTORS. J. Biol. Chem 278, 26715–26721. [PubMed: 12738796]
7. Kasuya Y, Umezawa H, and Hatano M (2018). Stress-Activated Protein Kinases in Spinal Cord Injury: Focus on Roles of p38. Int. J. Mol. Sci 19, 867. [PubMed: 29543752]
8. Premsrirut PK, Dow LE, Kim SY, Camiolo M, Malone CD, Miething C, Scuoppo C, Zuber J, Dickins RA, Kogan SC, et al. (2011). A Rapid and Scalable System for Studying Gene Function in Mice Using Conditional RNA Interference. Cell 145, 145–158. [PubMed: 21458673]
9. Nguyen AT, Dow AC, Kupiec-Weglinski J, Busuttil RW, and Lipshutz GS (2008). Evaluation of gene promoters for liver expression by hydrodynamic gene transfer. J. Surg. Res 148, 60–66. [PubMed: 18570932]
10. Kosuga M, Enosawa S, Li XK, Suzuki S, Matsuo N, Yamada M, Roy-Chowdhury J, Koiwai O, and Okuyama T (2000). Strong, long-term transgene expression in rat liver using chicken beta-actin promoter associated with cytomegalovirus immediate-early enhancer (CAG promoter). Cell Transplant. 9, 675–680. [PubMed: 11144964]
11. Cargnello M, and Roux PP (2011). Activation and function of the MAPKs and their substrates, the MAPK-activated protein kinases. Micro-biol. Mol. Biol. Rev 75, 50–83.
12. Shevchenko E, Poso A, and Pantsar T (2020). The autoinhibited state of MKK4: Phosphorylation, putative dimerization and R134W mutant studied by molecular dynamics simulations. Comput. Struct. Biotechnol. J 18, 2687–2698. [PubMed: 33101607]
13. Grompe M, Lindstedt S, Al-Dhalimy M, Kennaway NG, Papaconstantinou J, Torres-Ramos CA, Ou CN, and Finegold M (1995). Pharmacological correction of neonatal lethal hepatic dysfunction in a murine model of hereditary tyrosinaemia type I. Nat. Genet 10, 453–460. [PubMed: 7545495]
14. Marhenke S, Lamlé J, Buitrago-Molina LE, Cañón JMF, Geffers R, Finegold M, Sporn M, Yamamoto M, Manns MP, Grompe M, et al. (2008). Activation of nuclear factor E2-related factor 2 in hereditary tyrosinemia type 1 and its role in survival and tumor development. Hepatology 48, 487–496. [PubMed: 18666252]
15. Wolf MJ, Adili A, Piotrowitz K, Abdullah Z, Boege Y, Stemmer K, Ringelhan M, Simonavicius N, Egger M, Wohlleber D, et al. (2014). Metabolic activation of intrahepatic CD8+ T cells and NKT cells causes nonalcoholic steatohepatitis and liver cancer via cross-talk with hepatocytes. Cancer Cell 26, 549–564. [PubMed: 25314080]
16. Matsumoto T, Kinoshita T, Kirii Y, Tada T, and Yamano A (2012). Crystal and solution structures disclose a putative transient state of mitogen-activated protein kinase kinase 4. Biochem. Biophys. Res. Commun 425, 195–200. [PubMed: 22828509]
17. Matsumoto T, Kinoshita T, Kirii Y, Yokota K, Hamada K, and Tada T (2010). Crystal structures of MKK4 kinase domain reveal that substrate peptide binds to an allosteric site and induces an auto-inhibition state. Biochem. Biophys. Res. Commun 400, 369–373. [PubMed: 20732303]
18. Vin H, Ojeda SS, Ching G, Leung ML, Chitsazzadeh V, Dwyer DW, Adelmann CH, Restrepo M, Richards KN, Stewart LR, et al. (2013). BRAF inhibitors suppress apoptosis through off-target inhibition of JNK signaling. eLife 2, e00969. [PubMed: 24192036]
19. Klövekorn P, Pfaffenrot B, Juchum M, Selig R, Albrecht W, Zender L, and Laufer SA (2021). From off-to on-target: New BRAF-inhibitor-template-derived compounds selectively targeting mitogen activated protein kinase kinase 4 (MKK4). Eur. J. Med. Chem 210, 112963. [PubMed: 33199152]
20. Pfaffenrot B, Klövekorn P, Juchum M, Selig R, Albrecht W, Zender L, and Laufer SA (2021). Design and synthesis of 1H-pyrazolo[3,4-b]pyridines targeting mitogen-activated protein kinase kinase 4 (MKK4) - A promising target for liver regeneration. Eur. J. Med. Chem 218, 113371. [PubMed: 33794385]

21. Deibler KK, Mishra RK, Clutter MR, Antanasijevic A, Bergan R, Caffrey M, and Scheidt KA (2017). A Chemical Probe Strategy for Inter-rogating Inhibitor Selectivity Across the MEK Kinase Family. ACS Chem. Biol 12, 1245–1256. [PubMed: 28263556]
22. Bollag G, Hirth P, Tsai J, Zhang J, Ibrahim PN, Cho H, Spevak W, Zhang C, Zhang Y, Habets G, et al. (2010). Clinical efficacy of a RAF inhibitor needs broad target blockade in BRAF-mutant melanoma. Nature 467, 596–599. [PubMed: 20823850]
23. Karoulia Z, Wu Y, Ahmed TA, Xin Q, Bollard J, Krepler C, Wu X, Zhang C, Bollag G, Herlyn M, et al. (2016). An Integrated Model of RAF Inhibitor Action Predicts Inhibitor Activity against Oncogenic BRAF Signaling. Cancer Cell 30, 485–498. [PubMed: 27523909]
24. Mathea S, Abdul Azeez KRA, Salah E, Tallant C, Wolfreys F, Konietzny R, Fischer R, Lou HJ, Brennan PE, Schnapp G, et al. (2016). Structure of the Human Protein Kinase ZAK in Complex with Vemurafenib. ACS Chem. Biol 11, 1595–1602. [PubMed: 26999302]
25. Yang H, Young DW, Gusovsky F, and Chow JC (2000). Cellular Events Mediated by Lipopolysaccharide-stimulated Toll-like Receptor 4. MD-2 IS REQUIRED FOR ACTIVATION OF MITOGEN-ACTIVATED PROTEIN KINASES AND Elk-1. J. Biol. Chem 275, 20861–20866. [PubMed: 10877845]
26. Kodama Y, Taura K, Miura K, Schnabl B, Osawa Y, and Brenner DA (2009). Antiapoptotic effect of c-Jun N-terminal Kinase-1 through Mcl-1 stabilization in TNF-induced hepatocyte apoptosis. Gastroenterology 136, 1423–1434. [PubMed: 19249395]
27. Mohamed MR, Haybaeck J, Wu H, Su H, Bartneck M, Lin C, Boekschoten MV, Boor P, Goeppert B, Rupp C, et al. (2023). JNKs protect from cholestatic liver disease progression by modulating Apelin signalling. JHEP Rep. 5, 100854. [PubMed: 37791376]
28. Breitwieser W, Lyons S, Flenniken AM, Ashton G, Bruder G, Willington M, Lacaud G, Kouskoff V, and Jones N (2007). Feedback regulation of p38 activity via ATF2 is essential for survival of embryonic liver cells. Genes Dev. 21, 2069–2082. [PubMed: 17699753]
29. Gratton JP, Morales-Ruiz M, Kureishi Y, Fulton D, Walsh K, and Sessa WC (2001). Akt down-regulation of p38 signaling provides a novel mechanism of vascular endothelial growth factor-mediated cytoprotection in endothelial cells. J. Biol. Chem 276, 30359–30365. [PubMed: 11387313]
30. He G, and Karin M (2011). NF-κB and STAT3 – key players in liver inflammation and cancer. Cell Res. 21, 159–168. [PubMed: 21187858]
31. Verzella D, Pescatore A, Capece D, Vecchiotti D, Ursini MV, Franzoso G, Alesse E, and Zazzeroni F (2020). Life, death, and autophagy in cancer: NF-κB turns up everywhere. Cell Death Dis. 11, 210. [PubMed: 32231206]
32. Rinella ME, Lazarus JV, Ratziu V, Francque SM, Sanyal AJ, Kanwal F, Romero D, Abdelmalek MF, Anstee QM, Arab JP, et al. (2023). A multisociety Delphi consensus statement on new fatty liver disease nomenclature. J. Hepatol 79, 1542–1556. [PubMed: 37364790]
33. Yoshimoto S, Loo TM, Atarashi K, Kanda H, Sato S, Oyadomari S, Iwakura Y, Oshima K, Morita H, Hattori M, et al. (2013). Obesity-induced gut microbial metabolite promotes liver cancer through senescence secretome. Nature 499, 97–101. [PubMed: 23803760]
34. Febbraio MA, Reibe S, Shalapour S, Ooi GJ, Watt MJ, and Karin M (2019). Preclinical Models for Studying NASH-Driven HCC: How Useful Are They? Cell Metab. 29, 18–26. [PubMed: 30449681]
35. Toledo-Ibelles P, Gutiérrez-Vidal R, Calixto-Tlacomulco S, Delgado-Coello B, and Mas-Oliva J (2021). Hepatic Accumulation of Hypoxanthine: A Link Between Hyperuricemia and Nonalcoholic Fatty Liver Disease. Arch. Med. Res 52, 692–702. [PubMed: 33966916]
36. Li N, and Zhao H (2021). Role of Carnitine in Non-alcoholic Fatty Liver Disease and Other Related Diseases: An Update. Front. Med. (Lausanne) 8, 689042. [PubMed: 34434943]
37. Moon H, and Ro SW (2021). MAPK/ERK Signaling Pathway in Hepatocellular Carcinoma. Cancers (Basel) 13, 3026. [PubMed: 34204242]
38. Dhillon AS, Hagan S, Rath O, and Kolch W (2007). MAP kinase signalling pathways in cancer. Oncogene 26, 3279–3290. [PubMed: 17496922]

39. Rudalska R, Dauch D, Longerich T, McJunkin K, Wuestefeld T, Kang TW, Hohmeyer A, Pesic M, Leibold J, von Thun A, et al. (2014). In vivo RNAi screening identifies a mechanism of sorafenib resistance in liver cancer. Nat. Med 20, 1138–1146. [PubMed: 25216638]
40. Dauch D, Rudalska R, Cossa G, Nault JC, Kang TW, Wuestefeld T, Hohmeyer A, Imbeaud S, Yevsa T, Hoenicke L, et al. (2016). A MYC–aurora kinase A protein complex represents an actionable drug target in p53-altered liver cancer. Nat. Med 22, 744–753. [PubMed: 27213815]
41. Chen HS, Joo DJ, Shaheen M, Li Y, Wang Y, Yang J, Nicolas CT, Predmore K, Amiot B, Michalak G, et al. (2019). Randomized Trial of Spheroid Reservoir Bioartificial Liver in Porcine Model of Posthepatectomy Liver Failure. Hepatology 69, 329–342. [PubMed: 30022502]
42. Court FG, Laws PE, Morrison CP, Teague BD, Metcalfe MS, Wemyss-Holden SA, Dennison AR, and Maddern GJ (2004). Subtotal hepatectomy: a porcine model for the study of liver regeneration. J. Surg. Res 116, 181–186. [PubMed: 14732366]
43. Zhou H, Liu Z, Wang Y, Wen X, Amador EH, Yuan L, Ran X, Xiong L, Ran Y, Chen W, et al. (2022). Colorectal liver metastasis: molecular mechanism and interventional therapy. Signal Transduct. Target. Ther 7, 70. [PubMed: 35246503]
44. Xu F, Tang B, Jin TQ, and Dai CL (2018). Current status of surgical treatment of colorectal liver metastases. World J. Clin. Cases 6, 716–734. [PubMed: 30510936]
45. Yurekten O, Payne T, Tejera N, Amaladoss FX, Martin C, Williams M, and O'Donovan C (2024). MetaboLights: open data repository for metabolomics. Nucleic Acids Res. 52, D640–D646. [PubMed: 37971328]
46. Cai M, Huang Y, Yang R, Craigie R, and Clore GM (2016). A simple and robust protocol for high-yield expression of perdeuterated proteins in Escherichia coli grown in shaker flasks. J Biomol NMR 66, 85–91. [PubMed: 27709314]
47. Grompe M, Al-Dhalimy M, Finegold M, Ou CN, Burlingame T, Kennaway NG, and Soriano P (1993). Loss of fumarylacetoacetate hydrolase is responsible for the neonatal hepatic dysfunction phenotype of lethal albino mice. Genes Dev. 7, 2298–2307. [PubMed: 8253378]
48. Tugarinov V, and Kay LE (2004). An Isotope Labeling Strategy for Methyl TROSY Spectroscopy. J. Biomol. NMR 28, 165–172. [PubMed: 14755160]
49. Tugarinov V, Kanelis V, and Kay LE (2006). Isotope labeling strategies for the study of high-molecular-weight proteins by solution NMR spectroscopy. Nat. Protoc 1, 749–754. [PubMed: 17406304]
50. Ogura K, Terasawa H, and Inagaki F (1996). An improved double-tuned and isotope-filtered pulse scheme based on a pulsed field gradient and a wide-band inversion shaped pulse. J. Biomol. NMR 8, 492–498. [PubMed: 20859780]
51. Zwahlen C, Legault P, Vincent SJF, Greenblatt J, Konrat R, and Kay LE (1997). Methods for Measurement of Intermolecular NOEs by Multinuclear NMR Spectroscopy: Application to a Bacteriophage λ N-Peptide/boxB RNA Complex. J. Am. Chem. Soc 119, 6711–6721.
52. Breeze AL (2000). Isotope-filtered NMR methods for the study of biomolecular structure and interactions. Prog. Nucl. Magn. Reson. Spectrosc 36, 323–372.
53. Iwahara J, Wojciak JM, and Clubb RT (2001). Improved NMR spectra of a protein–DNA complex through rational mutagenesis and the application of a sensitivity optimized isotope-filtered NOESY experiment. J Biomol NMR 19, 231–241. [PubMed: 11330810]
54. Fesik SW, and Zuiderweg ERP (1988). Heteronuclear three-dimensional nmr spectroscopy. A strategy for the simplification of homonuclear two-dimensional NMR spectra. J. Magn. Reson. (1969) 78, 588–593.
55. Sinha K, Jen-Jacobson L, and Rule GS (2013). Divide and conquer is always best: sensitivity of methyl correlation experiments. J. Biomol. NMR 56, 331–335. [PubMed: 23771591]
56. Schanda P, Kupče E, and Brutscher B (2005). SOFAST-HMQC Experiments for Recording Two-dimensional Deteronuclear Correlation Spectra of Proteins within a Few Seconds. J Biomol NMR 33, 199–211. [PubMed: 16341750]
57. Güntert P, Mumenthaler C, and Wüthrich K (1997). Torsion angle dynamics for NMR structure calculation with the new program Dyana. J. Mol. Biol 273, 283–298. [PubMed: 9367762]
58. Schmidt E, and Güntert P (2012). A New Algorithm for Reliable and General NMR Resonance Assignment. J. Am. Chem. Soc 134, 12817–12829. [PubMed: 22794163]

59. Pronk S, Páll S, Schulz R, Larsson P, Bjelkmar P, Apostolov R, Shirts MR, Smith JC, Kasson PM, van der Spoel D.v.d., et al. (2013). GROMACS 4.5: a high-throughput and highly parallel open source molecular simulation toolkit. Bioinformatics 29, 845–854. [PubMed: 23407358]
60. Fabian MA, Biggs WH, Treiber DK, Atteridge CE, Azimioara MD, Benedetti MG, Carter TA, Ciceri P, Edeen PT, Floyd M, et al. (2005). A small molecule–kinase interaction map for clinical kinase inhibitors. Nat. Biotechnol 23, 329–336. [PubMed: 15711537]
61. Karaman MW, Herrgard S, Treiber DK, Gallant P, Atteridge CE, Campbell BT, Chan KW, Ciceri P, Davis MI, Edeen PT, et al. (2008). A quantitative analysis of kinase inhibitor selectivity. Nat. Biotechnol 26, 127–132. [PubMed: 18183025]
62. Nevzorova YA, Tolba R, Trautwein C, and Liedtke C (2015). Partial hepatectomy in mice. Lab Anim. 49 (Suppl), 81–88. [PubMed: 25835741]
63. Bertola A, Mathews S, Ki SH, Wang H, and Gao B (2013). Mouse model of chronic and binge ethanol feeding (the NIAAA model). Nat. Protoc 8, 627–637. [PubMed: 23449255]
64. Kang S, Elf S, Lythgoe K, Hitosugi T, Taunton J, Zhou W, Xiong L, Wang D, Muller S, Fan S, et al. (2010). p90 ribosomal S6 kinase 2 promotes invasion and metastasis of human head and neck squamous cell carcinoma cells. J. Clin. Invest 120, 1165–1177. [PubMed: 20234090]
65. Jiang H, Lei R, Ding SW, and Zhu S (2014). Skewer: a fast and accurate adapter trimmer for next-generation sequencing paired-end reads. BMC Bioinformatics 15, 182. [PubMed: 24925680]
66. Dobin A, Davis CA, Schlesinger F, Drenkow J, Zaleski C, Jha S, Batut P, Chaisson M, and Gingeras TR (2013). STAR: ultrafast universal RNA-seq aligner. Bioinformatics 29, 15–21. [PubMed: 23104886]
67. Love MI, Huber W, and Anders S (2014). Moderated estimation of fold change and dispersion for RNA-seq data with DESeq2. Genome Biol. 15, 550. [PubMed: 25516281]
68. R Core Team (2015). R: A Language and Environment for Statistical Computing (R Foundation for Statistical Computing). http://www.r-project.org/.
69. Benjamini Y, and Hochberg Y (1995). Controlling the False Discovery Rate: A Practical and Powerful Approach to Multiple Testing. J. R. Stat. Soc. B Methodol 57, 289–300.
70. Leuthold P, Schaeffeler E, Winter S, Büttner F, Hofmann U, Mürdter TE, Rausch S, Sonntag D, Wahrheit J, Fend F, et al. (2017). Comprehensive Metabolomic and Lipidomic Profiling of Human Kidney Tissue: A Platform Comparison. J. Proteome Res 16, 933–944. [PubMed: 27992229]
71. Tremmel R, Nies AT, van Eijck BAC, Handin N, Haag M, Winter S, Büttner FA, Kölz C, Klein F, Mazzola P, et al. (2022). Hepatic Expression of the Na^+-Taurocholate Cotransporting Polypeptide Is Independent from Genetic Variation. Int. J. Mol. Sci 23, 7468. [PubMed: 35806468]
72. Nies AT, König J, Leuthold P, Damme K, Winter S, Haag M, Masuda S, Kruck S, Daniel H, Spanier B, et al. (2023). Novel drug transporter substrates identification: An innovative approach based on metabolomic profiling, in silico ligand screening and biological validation. Pharmacol. Res 196, 106941. [PubMed: 37775020]
73. Smyth GK (2004). Linear models and empirical bayes methods for assessing differential expression in microarray experiments. Stat. Appl. Genet. Mol. Biol 3, Article3.
74. R Core Team (2014). R: A Language and Environment for Statistical Computing (R Foundation for Statistical Computing). http://www.r-project.org.
75. Phipson B, Lee S, Majewski IJ, Alexander WS, and Smyth GK (2016). ROBUST HYPERPARAMETER ESTIMATION PROTECTS AGAINST HYPERVARIABLE GENES AND IMPROVES POWER TO DETECT DIFFERENTIAL EXPRESSION. Ann. Appl. Stat 10, 946–963. [PubMed: 28367255]
76. Ritchie ME, Phipson B, Wu D, Hu Y, Law CW, Shi W, and Smyth GK (2015). limma powers differential expression analyses for RNA-sequencing and microarray studies. Nucleic Acids Res. 43, e47. [PubMed: 25605792]
77. Wickham H (2016). ggplot2: Elegant Graphics for Data Analysis (Springer).
78. Dührkop K, Fleischauer M, Ludwig M, Aksenov AA, Melnik AV, Meusel M, Dorrestein PC, Rousu J, and Böcker S (2019). SIRIUS 4: a rapid tool for turning tandem mass spectra into metabolite structure information. Nat. Methods 16, 299–302. [PubMed: 30886413]

79. Glorioso JM, Mao SA, Rodysill B, Mounajjed T, Kremers WK, Elgilani F, Hickey RD, Haugaa H, Rose CF, Amiot B, et al. (2015). Pivotal preclinical trial of the spheroid reservoir bioartificial liver. J. Hepatol 63, 388–398. [PubMed: 25817557]

80. Croome KP, Mao SA, Glorioso JM, Krishna M, Nyberg SL, and Nagorney DM (2015). Characterization of a porcine model for associating liver partition and portal vein ligation for a staged hepatectomy. HPB (Oxford) 17, 1130–1136. [PubMed: 26234167]

81. Shindoh J, Truty MJ, Aloia TA, Curley SA, Zimmitti G, Huang SY, Mahvash A, Gupta S, Wallace MJ, and Vauthey JN (2013). Kinetic growth rate after portal vein embolization predicts posthepatectomy outcomes: toward zero liver-related mortality in patients with colorectal liver metastases and small future liver remnant. J. Am. Coll. Surg 216, 201–209. [PubMed: 23219349]

82. Moser VC, McCormick JP, Creason JP, and MacPhail RC (1988). Comparison of chlordimeform and carbaryl using a functional observational battery. Fundam. Appl. Toxicol 11, 189–206. [PubMed: 3146518]

Highlights

- A first-in-class small-molecule-based MKK4 inhibitor was developed (HRX215)
- HRX215 increased liver regeneration after hepatectomy in murine and porcine models
- HRX215 treatment allowed for survival of pigs in a lethal 85% hepatectomy model
- A phase I trial revealed safety and excellent pharmacokinetics of HRX215 in humans

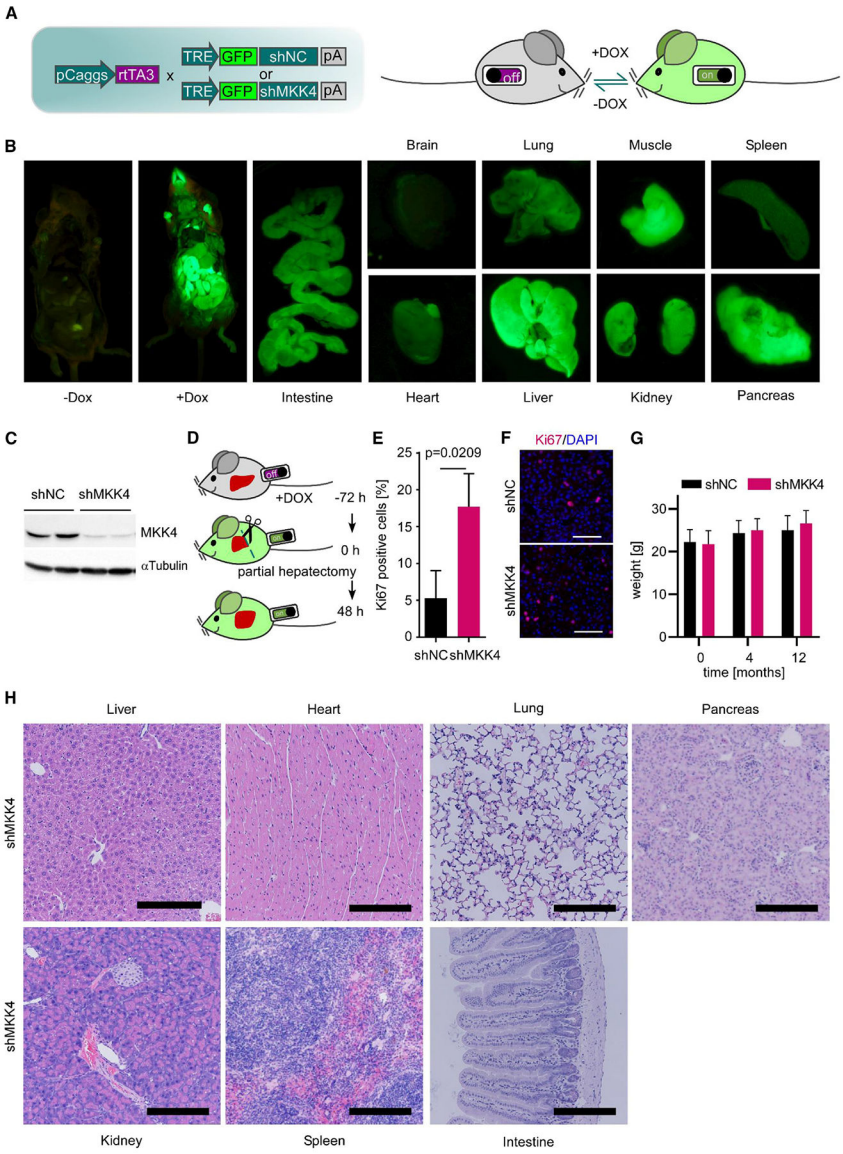

Figure 1. Genetic knockdown of MKK4 enhances liver regeneration and reveals long-term safety in mice

(A) Generation of shRNA-transgenic mice. TRE-GFP-shMKK4 or TRE-GFP-shNC mice were crossed with pCaggs-rtTA3 mice to enable dox-inducible ubiquitous MKK4 knockdown.

(B) Measurement of GFP expression as a surrogate marker for shRNA expression in the indicated organs after 3 days of dox administration. Shown are GFP fluorescence images of a representative mouse, three mice per group were analyzed.

(C) Immunoblot analysis reveals shRNA-mediated MKK4 knockdown in mouse livers after 5 days of dox administration (pooled lysates from two mouse livers).

(D) Partial hepatectomy (PH) experiments in shRNA transgenic mice. Dox was administered 72 h before PH. Mouse livers were harvested and analyzed 48 h after partial hepatectomy.

(E) Quantification of Ki67-positive cells on liver sections from shNC vs. shMKK4 mice. Statistical significance was calculated using unpaired t test (n = 3), p value: p = 0.0209. Mean + SD.

(F) Representative immunofluorescence images of merged Ki67 (pink) and DAPI (blue) stainings in shNC vs. shMKK4 murine livers under conditions as described in (E). Scale bars represent 200 μm.

(G) Body weight of shNC and shMKK4 mice during 12 months of continuous dox administration. Statistical significance was calculated using Sídák′s multiple comparison test (n = 3), p values: p = 0.9959 (0 months), p = 0.9898 (4 months), p = 0.8977 (12 months), mean + SD.

(H) Representative H&E stainings of indicated organs after 12 months of genetic MKK4 suppression. Scale bars represent 200 μm. See also Figure S1.

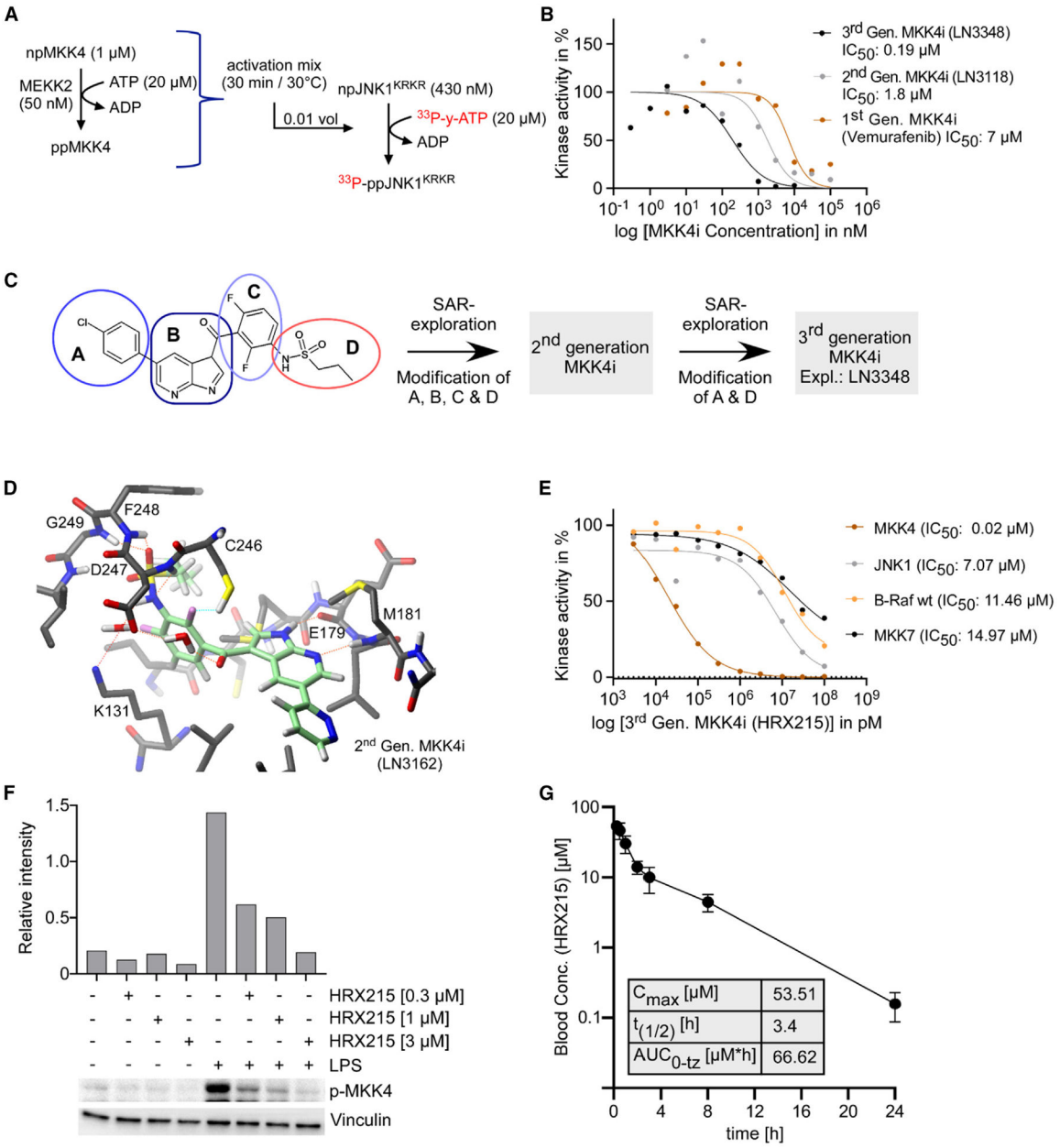

Figure 2. Development and characterization of potent and selective small molecule-MKK4 inhibitors

(A) A ^{33}P-y-ATP based cascade assay to quantify modulation of MKK4 activation upon compound binding measured by a ^{33}P-JNK readout.

(B) Dose-response relationships for the indicated 1st, 2nd, and 3rd generation MKK4 inhibitors as determined in a MKK4 radio-cascade assay. Concentrations were applied in singlicates.

(C) Overview of MKK4-inhibitor drug development starting with the chemical structure of vemurafenib that underwent modifications and eventually resulted in LN3348 (HRX215).

(D) Binding mode of LN3162 (pale green 3D-skeletal formula) at MKK4 (gray 3D-skeletal formula) as determined by NMR-spectroscopy. Involved amino acids are indicated. The cyan

dashed line indicates the tentative Cys-SH hydrogen bond with the ligand fluorine at the 2-position. The other H-bonds are shown as red dashed lines.

(E) HRX215 selectivity profile. Dose-response relationship for 10 concentrations (10^{-4} to 3×10^{-9} M) of HRX215 and kinase activity of MKK4, JNK1, BRAF, wild type (WT) and MKK7 in a radiometric protein kinase assay are shown. Concentrations were applied as singlicates.

(F) Target engagement assay with indicated concentrations of HRX215 conducted with isolated PBMCs. Lysates were analyzed by immunoblotting using an antibody against p-MKK4 (S257), and intensities were quantified (p-MKK4/Vinculin).

(G) Pharmacokinetics of HRX215 as determined in C57BL6/N WT mice. HRX215 was administered at 30 mg/kg per oral (p.o.) Blood concentrations of HRX215 were measured between 5 and 24 h (n = 3 each). Mean ± SD.

See also Figure S2.

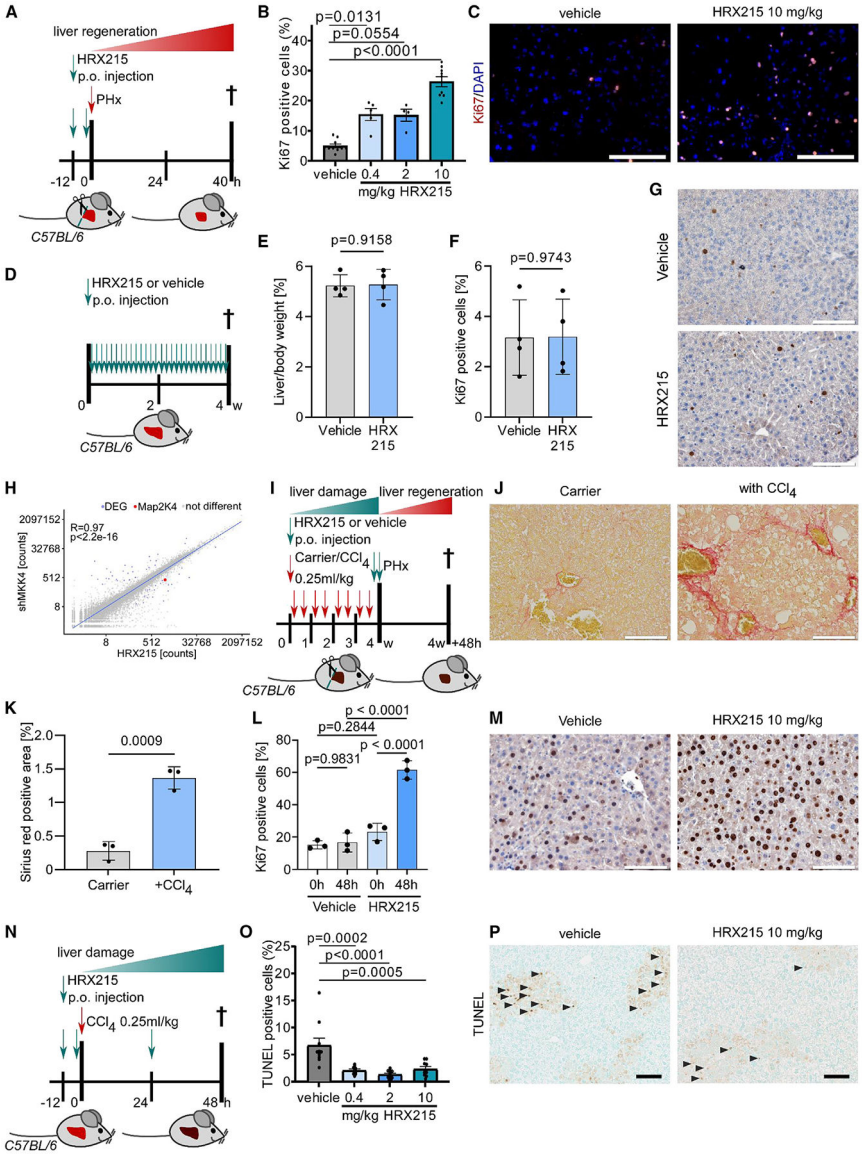

Figure 3. HRX215 increases hepatocyte proliferation upon partial hepatectomy and attenuates apoptosis in a CCl_4 liver damage model

(A) Partial hepatectomy (PH) experiments conducted in C57BL/6 WT mice treated with HRX215 (at 0.4, 2, 10 mg/kg) or vehicle (p.o.). Mice were euthanized after 48 h.

(B) Quantification of Ki67/DAPI stainings conducted on liver sections from mice as described in (A). Statistical significance was calculated using the Dunnett's multiple comparisons test (n ranged from 4 to 10 per group). p values: p = 0.0131 (0.4 mg/kg HRX215), p = 0.0554 (2 mg/kg HRX215), p < 0.0001 (10 mg/kg HRX215). Mean ± SEM.

(C) Representative images of the Ki67 (red) and DAPI (blue) stainings on liver sections from mice as described in (A). Ki67/DAPI stainings for vehicle (left) and HRX215 (10 mg/kg, right) are shown. Scale bars indicate 100 μm.

(D) C57BL/6 WT mice were treated with HRX215 (10 mg/kg) or vehicle via oral gavage daily. Mice were euthanized after 4 weeks.

(E) Analysis of liver to body weight ratio of mice treated as described in (D). Statistical significance was calculated using unpaired t test (n = 4). p value: p = 0.9158. Mean ± SD.
(F) Quantification of Ki67/hematoxylin immunohistochemistry stainings (positive cells in %) conducted on liver sections from mice as described in (D). Statistical significance was calculated using unpaired t test (n = 4). p value: p = 0.9743. Mean ± SD.
(G) Representative images of Ki67 (brown) and hematoxylin (blue) stainings on liver sections from mice as described in (D). Ki67/hematoxylin stainings for vehicle (left) and HRX215 (10 mg/kg, right) are shown. Scale bars represent 100 μm.
(H) Gene correlation analysis between shMKK4- and HRX215-treated mice (21,563 genes). 50 genes (differentially expressed genes (DEGs): blue dots) were significantly differentiated. Red dot: downregulated MKK4. RNA sequencing data were extracted from livers of shMKK4 mice or wild-type mice treated with HRX215 (10 mg/kg). Livers were harvested 48 h after PH and analyzed (n = 3). R: correlation coefficient; p value: $p < 2.2e^{16}$.
(I) CCl_4 liver-damage model combined with PH conducted in C57BL/6 WT mice treated with HRX215 (10 mg/kg) or vehicle via oral gavage. Mice were treated twice weekly over 3 weeks. HRX215 was administered 12 and 1 h prior to PH. Mice were euthanized 48 h after PH.
(J) Representative images of Sirius red stainings on liver sections from mice as described in (I). Sirius red staining without CCl_4 (left) and with CCl_4 (right) are shown. Scale bars represent 100 μm.
(K) Quantification of Sirus red staining (positive area in %) on liver sections from mice as described in (I). Statistical significance was calculated using unpaired t test (n = 3). p value: p = 0.0009. Mean ± SD.
(L) Quantification of Ki67/hematoxylin stainings (positive cells in %) conducted on liver sections from mice as described in (I). Statistical significance was calculated using the Tukey's multiple comparisons test (n = 3). p values: p = 0.9831, p = 0.2844, p < 0.0001 (0 vs. 48 h HRX215), p < 0.0001 (vehicle vs. HRX215 48 h). Mean ± SD.
(M) Representative images of the Ki67 (brown) and hematoxylin (blue) stainings on liver sections from mice as described in (I). Ki67/hematoxylin stainings for vehicle (left) and HRX215 10 mg/kg (right) are shown. Scale bars represent 100 μm.
(N) Schematic outline of a chemically induced (CCl_4) liver damage model conducted in C57BL/6 WT mice treated with HRX215 (at 0.4, 2, 10 mg/kg) or vehicle via oral gavage. Mice were euthanized after 48 h.
(O) Quantification of TUNEL stainings (positive cells in %) on liver sections from mice as described in (N). Statistical significance was calculated using the Dunnett's multiple comparisons test (n ranged from 9 to 10 per group). p values: p = 0.0002 (0.4 mg/kg HRX215), p < 0.0001 (2 mg/kg HRX215), p = 0.0005 (10 mg/kg HRX215). Mean + SEM.
(P) Representative images of TUNEL stainings on liver sections from mice as described in (N). TUNEL staining for vehicle (left) and HRX215 10 mg/kg (right) are shown. Arrows indicate TUNEL-positive cells (brown). Scale bars indicate 100 μm.
See also Figures S3 and S4.

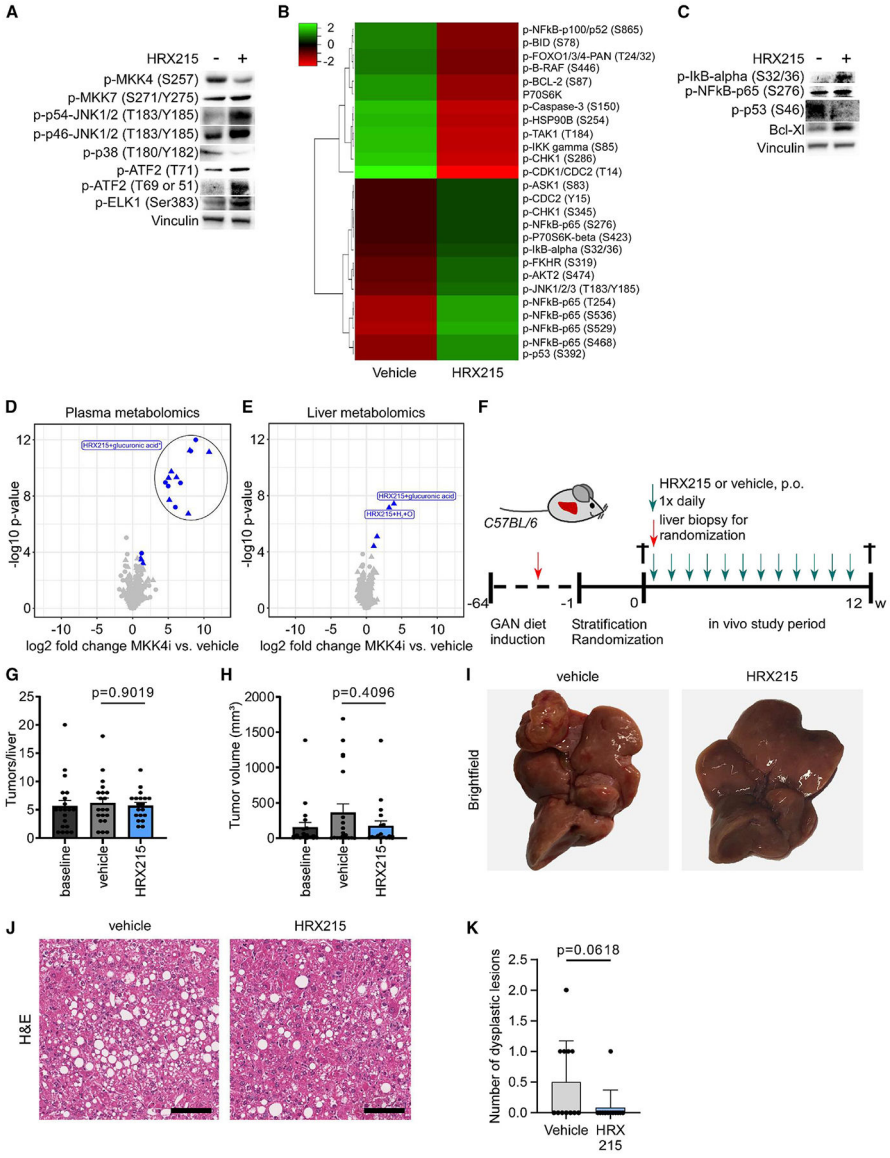

Figure 4. Safety of long-term HRX215 treatment

(A) Immunoblot analysis of MAPK signaling cascade under HRX215 treatment in hepatectomized mice. 10 mg/kg HRX215 were administered to mice 8 and 1 h prior to partial hepatectomy (PH). Mice were euthanized 1 h after PH. Pooled lysates from four mouse livers were analyzed each. DMSO is indicated as " " and HRX215 as "+."

(B) Apoptosis phosphoprotein array analysis from whole-cell protein lysates extracted 48 h after PH from livers treated with either vehicle or HRX215. HRX215 or vehicle was administered 12 and 1 h prior to PH. Mice were euthanized 48 h after PH. Pooled lysates from three mouse livers were analyzed 48 h after PH. Top increased (green) and decreased (red) phosphorylated proteins are shown as heat map visualization and were calculated as $\log_2$-fold changes. Hierarchical clustering relationship between analyzed factors (left).

(C) Immunoblot analysis of anti-apoptotic proteins in hepatectomized mouse livers under HRX215 treatment. 10 mg/kg HRX215 or vehicle was administered 12 and 1 h prior to PH.

Mice were euthanized 48 h after PH. Pooled lysates from three mouse livers were analyzed 48 h after PH. DMSO is indicated as " " and HRX215 is indicated as "+."

(D and E) Nontargeted metabolomics analyses of differentially regulated features in plasma (D) and liver (E) samples between HRX215- and vehicle-treated mice. 1,337 features were found in plasma samples and 814 features in liver tissue. Volcano plots show $\log_2$-fold changes vs. Benjamini-Hochberg adjusted p values ($-\log_{10}$ transformed). Features with an absolute $\log_2$-fold change ≥ 1 and an adjusted p value < 0.05 are colored in blue. Structurally annotated metabolites are labeled with the corresponding name, whereas unassigned metabolites were not labeled. Gray dots represent features that were not significantly altered. Features detected in positive ionization mode are shown as triangles, whereas features detected in negative ionization mode are shown as circles. *HRX215-glucuronide was detected as multiple ESI-MS ionization adducts in plasma samples.

(F) GAN-NASH HCC model conducted in C57BL/6 WT mice treated with HRX215 or vehicle (daily treatment via oral gavage over 12 weeks after 63 weeks of GAN diet). Mice were euthanized after a total of 76 weeks.

(G) Quantification of tumors per liver in harvested mouse livers as described in (F). Tumors per liver at baseline were compared between vehicle and HRX215 treated mice. Statistical significance was calculated using the Dunnett's multiple comparisons test (n = 19–20). p value: p = 0.9019. Mean + SEM.

(H) Quantification of average tumor nodule volume (mm^2) in harvested mouse livers as described in (F). Tumor volumes at baseline were compared with vehicle- and HRX 215-treated mice. Statistical significance was calculated using the Dunnett's multiple comparisons test (n = 19–20). p value: p = 0.4096. Mean + SEM.

(I) Bright-field images of representative livers from wild-type mice in (F) treated with vehicle (left) or HRX215 (right).

(J) H&E stainings of representative livers from wild-type mice in (F) treated with vehicle (left) or HRX215 (right). Scale bars indicate 100 μm.

(K) Quantification of dysplastic lesions in vehicle- or HRX215-treated livers from mice used in (F). Statistical analysis was conducted using unpaired t test (n = 12). p value: p = 0.0618. Mean + SD.

See also Figures S4–S6.

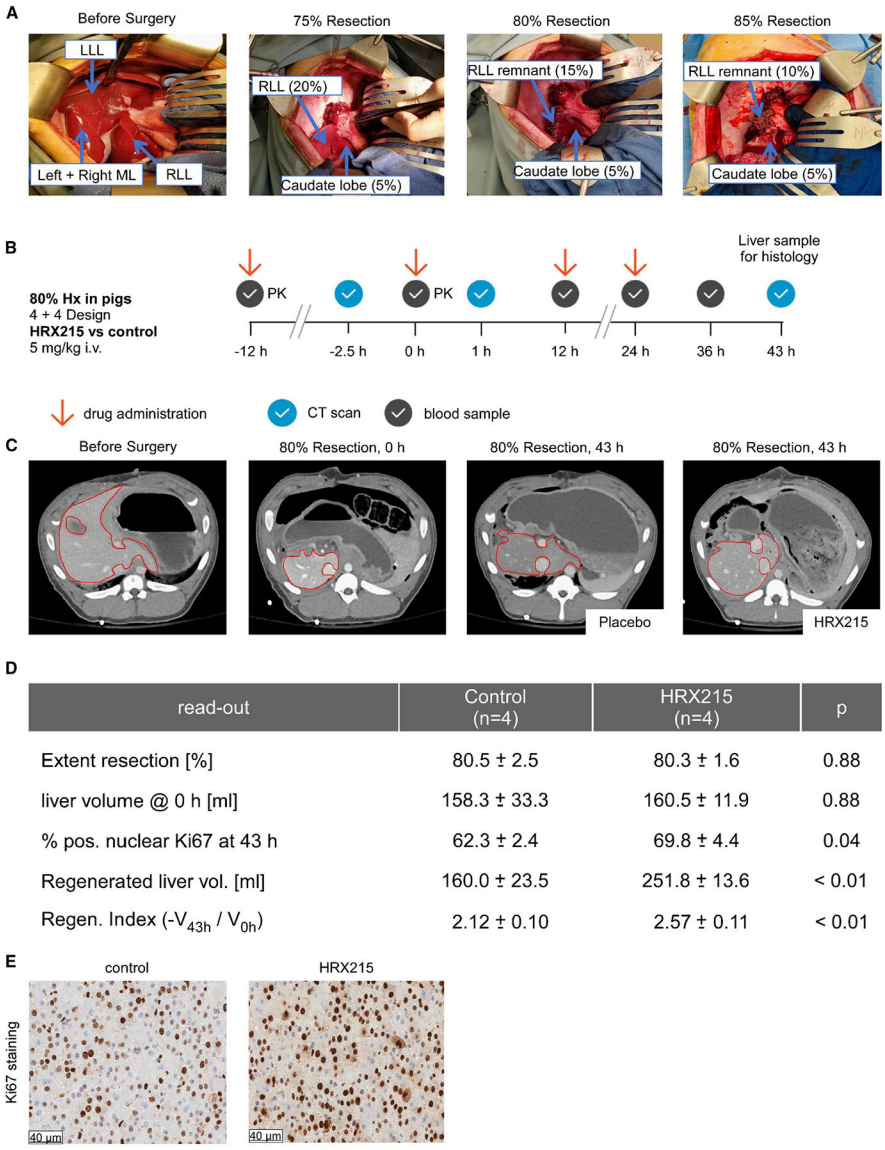

read-out	Control (n=4)	HRX215 (n=4)	p
Extent resection [%]	80.5 ± 2.5	80.3 ± 1.6	0.88
liver volume @ 0 h [ml]	158.3 ± 33.3	160.5 ± 11.9	0.88
% pos. nuclear Ki67 at 43 h	62.3 ± 2.4	69.8 ± 4.4	0.04
Regenerated liver vol. [ml]	160.0 ± 23.5	251.8 ± 13.6	< 0.01
Regen. Index ($-V_{43h} / V_{0h}$)	2.12 ± 0.10	2.57 ± 0.11	< 0.01

Figure 5. HRX215 increases liver regeneration after 80% hepatectomy in pigs

(A) Photographs of situs before and after surgery (75%, 80%, and 85% resection) of porcine livers are depicted showing the remnant liver volume. LL, left liver lobe; M, middle lobe; RLL, right liver lobe.

(B) 80% hepatectomy study in pigs treated with HRX215 (5 mg/kg intravenous [i.v.]) or vehicle at indicated time points (red arrow). During the indicated time course, CT scans (blue circles) and blood sampling (gray circles) were conducted. Pigs were euthanized 43 h after surgery.

(C) CT scans before and after 80% PH at time point 0 and 43 h are shown. The liver (circled with dashed red line) of a carrier-treated pig is shown in direct comparison with the liver of an HRX 215-treated pig.

(D) Quantification of liver volumes, extent of resection, and newly regenerated liver volume at indicated time points comparing control-treated with HRX 215-treated pigs.

(E) Ki67 stainings on liver sections from control- (left) or HRX215 (right)-treated pigs. Ki67-positive cells are depicted in brown. Scale bar represents 40 μm.

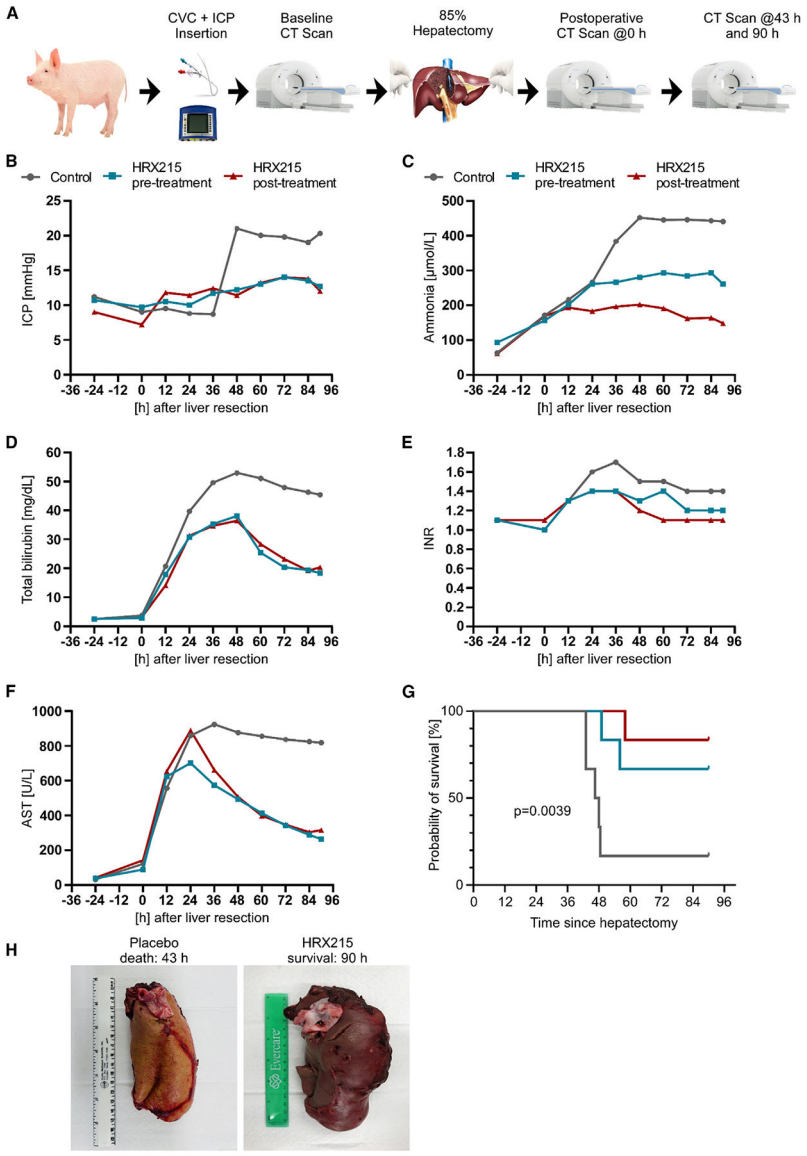

Figure 6. HRX215 prevents liver failure after 85% hepatectomy

(A–F) (A) Experimental setup for porcine 85% hepatectomy experiments (B–F). Kinetics of intracranial pressure (ICP), ammonia, total bilirubin, INR, and aspartate aminotransferase (AST) over 120 h are shown (for pre- and post-liver resection treatment groups). Pigs received either carrier treatment (gray), HRX215 pre-surgery treatment (cyan), or HRX215 post-surgery treatment (red) (n = 6).

(G) Survival of pigs that either received placebo (gray), HRX215 pre-surgery treatment (cyan), or HRX215 post-surgery treatment (red). Statistical significance was calculated using the log-rank (Mantel-Cox) test (n = 6). p value: p = 0.0039.

(H) Representative images of a liver from a carrier- (left) or HRX215- (right) treated pig.

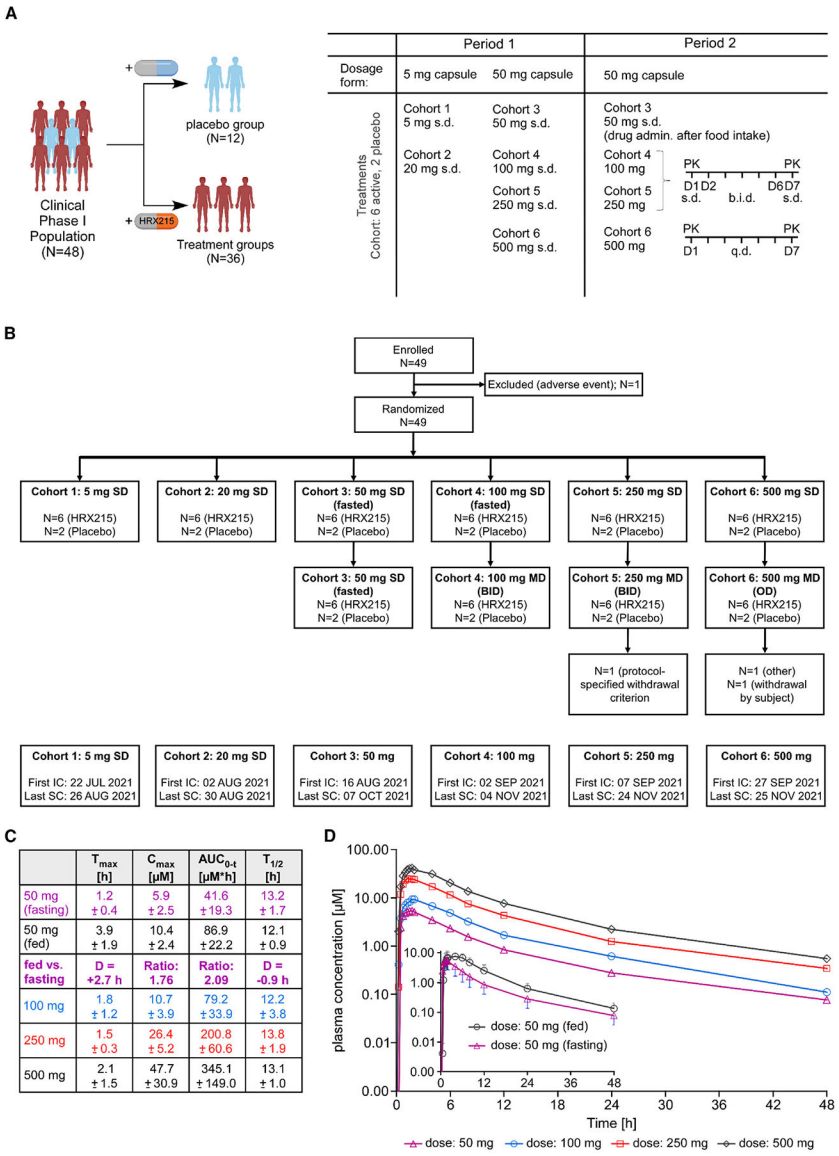

	T_{max} [h]	C_{max} [µM]	AUC_{0-t} [µM*h]	$T_{1/2}$ [h]
50 mg (fasting)	1.2 ± 0.4	5.9 ± 2.5	41.6 ± 19.3	13.2 ± 1.7
50 mg (fed)	3.9 ± 1.9	10.4 ± 2.4	86.9 ± 22.2	12.1 ± 0.9
fed vs. fasting	**D = +2.7 h**	**Ratio: 1.76**	**Ratio: 2.09**	**D = -0.9 h**
100 mg	1.8 ± 1.2	10.7 ± 3.9	79.2 ± 33.9	12.2 ± 3.8
250 mg	1.5 ± 0.3	26.4 ± 5.2	200.8 ± 60.6	13.8 ± 1.9
500 mg	2.1 ± 1.5	47.7 ± 30.9	345.1 ± 149.0	13.1 ± 1.0

Figure 7. First-in-human (FIH) phase I clinical trial with HRX215

(A) Schematic outline of the trial illustrating the placebo (n = 12) and HRX215 treatment (n = 36) groups (left). Dosage scheme of the 6 active and 2 placebo cohorts included into the FIH study (right). Cohorts received 5–500 mg HRX215 as a single dose (s.d.) under fasting conditions during the first period. In period 2, single doses of 50 mg during fed conditions and multiple ascending doses of 100 and 250 mg HRX215 twice a day (b.i.d.) and 500 mg HRX215 once a day (q.d.) were administered.

(B) Consolidated Standards of Reporting Trials (CONSORT) flow diagram.

(C) Parameters of the s.d. pharmacokinetics (100, 250, and 500 mg) and the fed (black) vs. fasting (purple) conditions.

(D) Pharmacokinetic profiles of HRX215 in the plasma after single dosages of 50–500 mg and 50 mg under fed (black) vs. fasting (purple) conditions. Mean ± SD. See also Figure S7.

KEY RESOURCES TABLE

REAGENT or RESOURCE	SOURCE	IDENTIFIER
Antibodies		
p-MKK4 (S257)	Cell Signaling Technology	CST4514: RRID:AB_2140946
MKK4	Cell Signaling Technology	CST9152: RRID:AB_330905
MKK4	Abcam	ab33912: RRID:AB_776381
p-MKK7 (S271/Y275)	Bioss	BS-3277R: RRID:AB_10855821
α-Tubulin	Cell Signaling Technology	CST2125: RRID:AB_2619646
Vinculin	Sigma	V9131: RRID:AB_477629
p-JNK1/2 (T183/Y185)	Cell Signaling Technology	CST4668: RRID:AB_823588
p-p38 (T180/Y182)	Cell Signaling Technology	CST4511: RRID:AB_2139682
p-ATF2 (T69 or 51)	Abcam	ab131106: RRID:AB_11157608
p-ATF2 (T71)	Abcam	ab32019: RRID:AB_725567
p-Elk1 (S383)	Cell Signaling Technology	CST9181: RRID:AB_2099016
p-IκB alpha (S32)	Cell Signaling Technology	CST2859: RRID:AB_561111
p-NFκB-p65 (S276)	GeneTex	GTX54672: RRID:AB_3094748
p-p53 (S46)	Cell Signaling Technology	CST2521: RRID:AB_10828689
Bcl-XL	Cell Signaling Technology	CST2764: RRID:AB_2228008
Cdc25c	Cell Signaling Technology	CST4688: RRID:AB_560956
CDK4	Abcam	ab137675: RRID:AB_3094750
Cyclin A2	Abcam	ab38: RRID:AB_304084
Cyclin B1	Cell Signaling Technology	CST4138: RRID:AB_2072132
Cyclin E1	Cell Signaling Technology	CST20808: RRID:AB_2783554
Cyclin D1	Cell Signaling Technology	CST2922: RRID:AB_2228523
Stathmin	Cell Signaling Technology	CST13655: RRID:AB_2798284
EGFR	Cell Signaling Technology	CST2232: RRID:AB_331707
HER2/ErbB2	Cell Signaling Technology	CST4290: RRID:AB_10557104
p-ERK1/2 (T202/Y204)	Cell Signaling Technology	CST9101: RRID:AB_331646
Ki67	Abcam	ab15580: RRID:AB_443209
α-SMA	Sigma	A2547: RRID:AB_476701
p21	Sigma-Aldrich	ZRB1141: RRID:AB_3094752
γH2Ax (S139)	Cell Signaling	CST9718: RRID:AB_2118009

REAGENT or RESOURCE	SOURCE	IDENTIFIER
Anti-mouse secondary antibody	Dianova	115-035-062: RRID:AB_2338504
Anti-rabbit secondary antibody	Dianova	111-035-045: RRID:AB_2337938
Bacterial and virus strains		
E. coli BL21 (D3)	Thermo Fischer Scientific	EC0114
Chemicals, peptides, and recombinant proteins		
CCl_4	Sigma-Aldrich	289116
D-Sorbitol	Sigma-Aldrich	S1876
LPS *E.coli* O26:B6	Sigma-Aldrich	L8274
Clarity Western ECL Substrate	BioRad	1705061
DAB substrate Kit	Zytomed	DAB-057
MKK4	ProQinase	0948-0000-2
Single mutants of MILV residues	ZoBio B.V.	N/A
Trypan blue solution	Sigma-Aldrich	93595
Crystal violet	Sigma-Aldrich	C6158
Hematoxylin solution A+B	Roth	X906, X907
Direct red 80	Sigma-Aldrich	2610-10-8
Critical commercial assays		
Apoptosis Phospho Antibody Array	Full moon Biosystems	PAP247
In Situ Cell Death Detection Kit, TMR red	Roche	12156792910
DC Protein Assay Kit	BioRad	5000111
ProQinase activity assay	ProQinase	N/A
MagMAX™ mirVana™ Total RNA Isolation Kit	Thermo Fischer Scientific	A27828
TruSeq Stranded mRNA kit	Illumina	20020594
Deposited data		
mRNA seq	ENA	ENA: PRJEB72069 (https://www.ebi.ac.uk/ena/browser/view/PRJEB72069).
metabolomics	MetaboLights	MetaboLights: MTBLS9434 (www.ebi.ac.uk/metabolights/MTBLS9434)
First-In-Human Phase I study	Zenodo	Zenodo:https://doi.org/10.5281/zenodo.10558364
Experimental models: Cell lines		
Sf9 insect cells	Sigma-Aldrich	71104
HEK-293	ATCC	CRL-1573
Nras^{G12V};*Cdkn2a*$^{ARF-/-}$ HCC cells	Zender Lab	N/A
Nras^{G12V};*Trp53*$^{-/-}$ HCC cells	Zender Lab	N/A
Experimental models: Organisms/ strains		
B6.129S4-Tg(Col1AMAP2K4.3278)1MRS mice	Mirimus Inc	N/A
B6N.FVB(Cg)-Tg(CAG-rtTA394288Slowe/J mice	Mirimus Inc	N/A

REAGENT or RESOURCE	SOURCE	IDENTIFIER
TRE GFP shRen.713 (B6.129S4-Tg(Col1A-REN.713) 1MRS mice	Mirimus Inc	N/A
FAH$^{-/-}$ (B6.Fahtm1Mgo) mice	Markus Grompe Lab	N/A
Recombinant DNA		
pCaggs-FAH-IRES-GFP-shNC	This paper	N/A
pCaggs-FAH-IRES-GFP-shMKK4	This paper	N/A
pET22b+	Sigma-Aldrich	69744
Software and algorithms		
ImageJ	Open source	https://imagej.net/software/fiji/
GraphPad Prism 9.4.1	Dotmatics	https://www.graphpad.com/how-to-buy/
Heatmapper	Open source	http://www.heatmapper.ca/expression/
R (version 4.0.4)	R Core team	N/A
GROMACS	GROMACS development team	https://www.gromacs.org/
DESeq2 (version 1.24.0)	Bioconductor	https://bioconductor.org/packages/release/bioc/html/DESeq2.html
CYANA	ZoBio R.V.	N/A
Other		
KINOMEscan™	DiscoveRx/ Eurofins	https://www.eurofinsdiscovery.com/solution/kinomescan-technology?gclid=EAIaIQobChMIiq30kYPRggMVcYVoCR26NAI0EAAYAiAAEgK0dvD_BwE
Dox food	Sniff	A112-D70620
CD-HFD	Research Diets	D05010402